Keep Calm and Baryon: The Distribution of Baryons and Dark Matter on Cosmic Scales

Benjamin A. Cook

Advisor: Prof. Neta Bahcall

Submitted in partial fulfillment
of the requirements for the degree of
Bachelor of Arts
Department of Astrophysical Sciences
Princeton University

May 2014

I hereby declare that I am the sole author of this thesis.

I authorize Princeton University to lend this thesis to other institutions or individuals for the purpose of scholarly research.

Benjamin A. Cook

I further authorize Princeton University to reproduce this thesis by photocopying or by other means, in total or in part, at the request of other institutions or individuals for the purpose of scholarly research.

Benjamin A. Cook

Abstract

We present a compilation of observational constraints on the distribution of baryons, relative to dark matter, in cosmic halos ranging from galaxies to massive clusters. These include X-ray and SZ measurements of the hot intracluster medium (ICM) in groups and clusters, weak lensing and optical constraints on the cluster stellar fraction, and absorption measurements of the cool circumgalactic medium (CGM) outside galaxies. Using direct observations when possible and extrapolations of observed density profiles when necessary, we show that the baryon content within the virial radius matches the cosmic baryon fraction (0.164) for halos ranging over three orders of magnitude in mass. The baryonic mass is therefore a strong tracer of the underlying dark matter distribution, and can be used as a tool in cosmological studies of structure formation, although baryons are more extended beyond the virial radius in low-mass halos. Using the ratio of stellar fractions in galaxies and clusters, we place a lower limit of 40% on the contributions of individual galaxy halos to the dark matter and baryonic mass of clusters.

Acknowledgements

Thank Prof. Prochaska, and Lars/Shy and Carlstrom/Plagge if they get back to me.

Dedicated to my brother, Walter.

Contents

Chapter 1

Introduction

1.1 The Cosmic Baryon Fraction

In the beginning, there was the big bang. All of the contributions to the cosmic energy budget – all of the forms that matter and energy take today – originated around 13.8 billion years ago, when the universe was unimaginably hot and dense. Various mechanisms[1] have been offered to explain the genesis of the energy-filled, rapidly expanding universe which appeared in the briefest fraction of a second after the big bang. As the universe expanded and cooled, the available energy distributed itself into various different forms, eventually settling down into the primary energy components we observe today, including radiation (photons and neutrinos), baryons ("ordinary" matter, comprised of protons, neutrons, and electrons), as well as the mysterious dark matter and dark energy.

Energy did not populate these forms in equal proportions; the energy densities of each population differed by many orders of magnitude, initially, and their ratios changed continually throughout the expansion history of the universe. Radiation density – primarily the photon density (ρ_γ), dominant in the earliest periods after

[1] most notably the theory of inflation, which will surely see a dramatic increase in interest since the detections of B-mode polarization in the CMB (BICEP2 Collaboration et al., 2014).

the big bang – diluted quickly from the combination of expansionary volume increase and Doppler redshifting. The matter density – ρ_m, comprised of both baryons (ρ_b) and cold dark matter (ρ_c) – was initially only a minuscule portion of the cosmic energy budget, but eventually matter dominated the cosmic scene after expansion "cooled" the photon temperature significantly. Buried far below the other components originally, dark energy – ρ_ν, commonly thought to be a cosmological constant Λ – retains a constant energy density while the universe expands, becoming dominant at late times when ρ_m has decreased significantly. Each of these energy densities are often scaled by the critical density required to stop cosmic expansion: $\rho_{crit} = \frac{8}{3}\pi G \mathrm{H_0}^2 c^{-2}$, with $\mathrm{H_0}$ the Hubble constant, G Newton's constant, and c the speed of light. The density of each component relative to the critical density is expressed as Ω, for example:

$$\frac{\rho_b}{\rho_{crit}} = \Omega_b.$$

Baryons and dark matter, the two components of the total matter density, have the same dependence on the expansionary scale factor and redshift. Since the total matter density is just their sum, the total matter density also scales identically:

$$\begin{aligned} \rho_c \propto \rho_b \propto \rho_m &\propto \mathrm{a}^{-3} \\ &\propto (1+\mathrm{z})^3. \end{aligned}$$

Therefore, we see that the ratio of baryons to dark matter will remain constant from its primordial level throughout the history of the universe. A more useful and commonly studied constant is the *cosmic baryon fraction*, f_b, the fraction of all matter in baryonic form:

$$\mathrm{f}_b = \frac{\rho_b}{\rho_b + \rho_c} = \frac{\rho_b}{\rho_m} = \frac{\Omega_b}{\Omega_m}. \tag{1.1}$$

The above argument, that the baryon fraction remains constant throughout cosmic history, applies only in the homogeneous regime, where there are no spatial variations in the overall mass density. When inhomogeneities exist, self-interactions lead to the complicated evolution of structure. Both baryons and dark matter are subject to gravitational forces, causing initial overdensities to increase in magnitude, eventually collapsing into massive halos. Yet while dark matter primarily interacts only through gravity, baryons are subject to electromagnetic forces, thermal emission, and numerous other interactions that lead to a divergence between the dark matter distribution and the baryon distribution.

While both dark matter and baryons cause the gravitational collapse of inhomogeneities and drive the growth of structure, it is obvious that the baryon fraction plays an incredibly important role in determining the makeup of our universe. Baryons are responsible for all other phenomena studied in physics and astrophysics: the formation of galaxies and stars, supernovae, photon radiation, and, eventually, life itself. Although the local baryon fraction may vary hugely from place to place, it is possible to estimate the cosmic baryon fraction by averaging over a substantially large volume. This cosmic ratio is a defining characteristic, and studying it is essential to properly understanding the creation and evolution of our universe. THIS SECTION CAN USE SOME MAJOR WORK. NARROW THE FOCUS, BUT STILL GIVE IT SOME DEPTH.

The baryon fraction was a major factor in several important physical processes in the early universe. Through observable consequences of these processes, cosmologists have been able to place powerful constraints on the cosmic baryon fraction at these early times. Consistent with the literature, we will consider the baryon fraction inferred from these methods to be the "true" cosmic fraction against which we will compare measurements from the local, highly inhomogeneous universe.

One such mechanism is big bang nucleosynthesis (BBN), which generated the first light elements beyond hydrogen[2]. In the first seconds after the big bang, the only

[2]The discussion which follows is guided primarily by chapter 3.2 of Weinberg (2008), a useful but relatively technical reference on the topic.

ordinary matter particles which existed (and were stable) were protons (p), electrons (e), and neutrons (n). The high temperatures and densities of nucleons allowed the conversion of protons and neutrons into more complex and heavier nuclei, through processes such as:

$$p + n \to d + \gamma$$
$$d + d \to {}^3\mathrm{He} + n$$
$$d + {}^3\mathrm{He} \to {}^4\mathrm{He} + p.$$

The BBN reactions began around 100 – 200 seconds after the big bang (Weinberg, 2008). The exact time when these reactions reached thermal equilibrium depends weakly on the abundance of baryons, $\Omega_b h^2$, where $\mathrm{H}_0 = 100h$ km s^{-1} Mpc^{-1} defines h, an important scaling factor[3]. After the universe expanded and cooled sufficiently, these reactions fell out of equilibrium, leaving the universe enriched with helium (^{4}He and ^{3}He) and trace amounts of elements such as deuterium (d) and lithium (^{7}Li). The transformation of n and d into helium is more complete the higher $\Omega_b h^2$. Therefore, the baryon abundance strongly affects the resulting abundance of d and residual elements like lithium and ^{3}He. Figure 1.1 shows the dependence of these primordial abundances on the cosmic baryon abundance.

The baryon abundance can be determined through observational constraints of, for example, the deuterium abundance, which among the common byproducts of BBN depends most strongly on $\Omega_b h^2$. The deuterium abundance has been inferred from variety of sources, including from the Milky Way's ISM (Linsky et al., 1993, 1995), absorption towards QSOs (Tytler et al., 1996; Kirkman et al., 2003), and even from measurements of the composition of the Jovian atmosphere (Niemann et al.,

[3]Uncertainties on the true expansion rate (h) translate into uncertainties on a number of observables such as matter abundances (Ω) and halo properties (M, r). Therefore, many derived properties in the literature are often given in terms of $h_{72} \equiv \mathrm{H}_0/72$ km s^{-1} Mpc^{-1}.

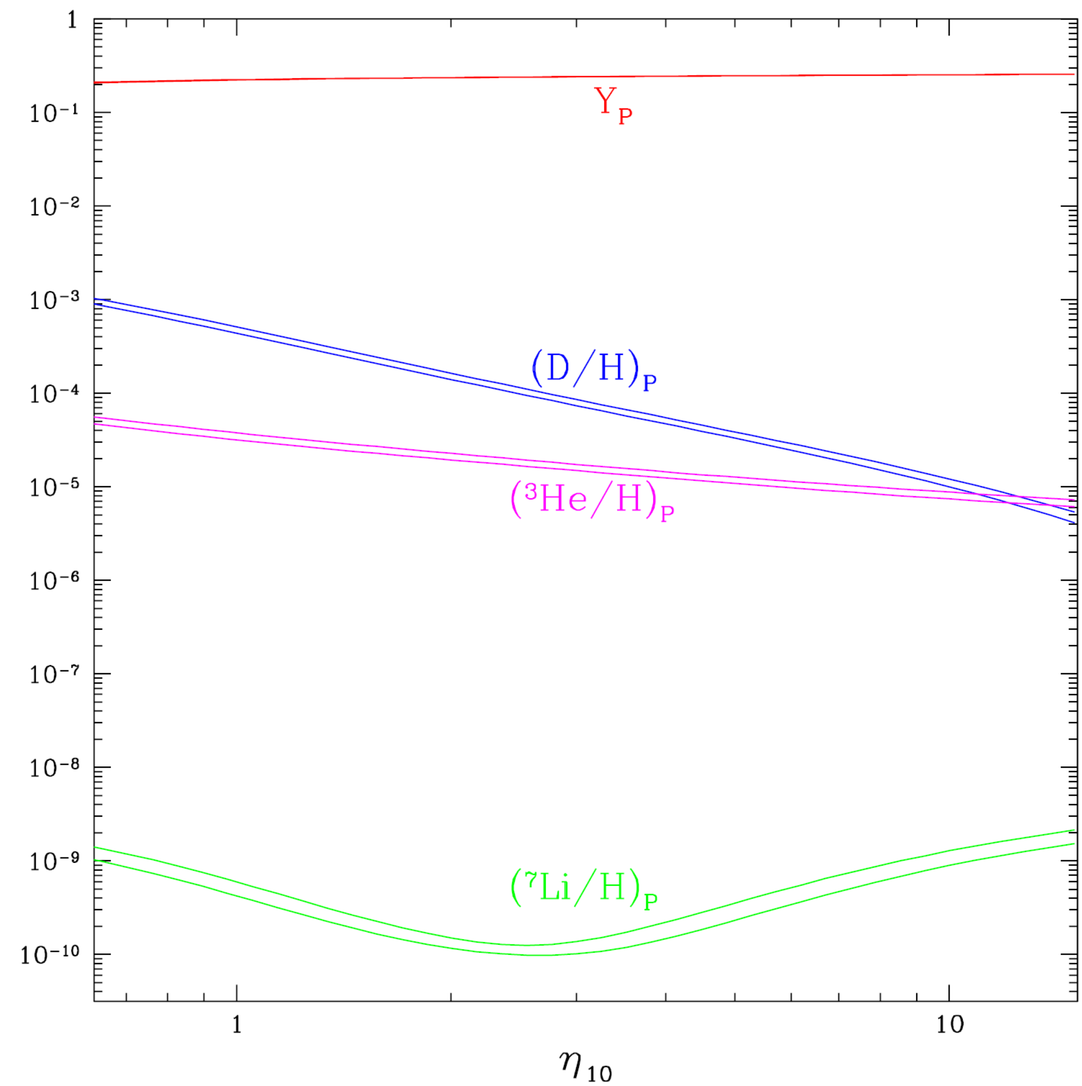

Figure 1.1: The BBN-predicted primordial abundances of deuterium (D), ^{3}He, ^{7}Li, and ^{4}He (Y_P), as a function of the baryon abundance parameter $\eta_{10} \sim 274 \times \Omega_b h^2$. The width of the curves represents the uncertainties in various nuclear reaction rates. Figure taken from Steigman (2006, Fig. 1), another helpful overview of BBN physics.

1996). All such methods have limitations, as deuterium can be destroyed in stellar (and brown dwarf) cores, altering the deuterium abundance slightly with time. Iocco et al. (2009) provides a modern compilation of deuterium abundance measurements, placing the constraint on the baryon abundance at $\Omega_b h^2 = 0.021 \pm 0.001$. Observed ^{7}Li abundances are a factor of a few lower than predicted from BBN, suggesting that there could be additional physics responsible for destroying lithium (Suzuki et al., 2000; Meléndez & Ramírez, 2004). This is known as the "Lithium Problem," and is still an unsolved problem in interpreting BBN.

A complementary method of inferring the baryon abundance at early times is from measurements of the acoustic peaks in the Cosmic Microwave Background (CMB) power spectrum. Remember that the CMB power spectrum contains large peaks, representing correlations in the CMB on particular scales. In the first few hundred thousand years[4] after the big bang, the temperature of the universe was high enough to keep atoms fully ionized into separate nuclei and electrons. These charged particles were strongly coupled to the photons through electromagnetic interactions, so that the two combined to form what is called a photon-baryon fluid. This fluid (which, at the time, had an energy density around $\frac{1}{3}$ that of dark matter) fell towards the centers of gravitational wells created by dark matter. However, unlike the non-interacting dark matter, the photon-baryon fluid's pressure rose when its density rose, forcing the fluid out of the well until its pressure dropped enough to allow gravity to draw it back once again. These ongoing fluctuations in the pressure and density of the fluid were frozen into the CMB when the average temperature of the universe dropped sufficiently to allow neutral atoms to form, and the CMB photons began streaming freely through the universe[5].

The baryon abundance at this early time had several effects on the acoustic peaks

[4]Virtually a cosmic blink of the eye.

[5]For a good, low-level introduction to the concept of acoustic peaks in the CMB, see Chapter 9 of Ryden (2003).

in the CMB, as did the overall mass abundance ($\Omega_m h^2$). Figure 1.2 shows how changes in these abundances are reflected in the acoustic peaks. The location of the first peak (and all subsequent peaks) is determined by the sound speed at the epoch of last scattering. This sound speed increases when $\Omega_b h^2$ increases, but is more sensitive to changes in $\Omega_m h^2$, an increase of which results in a decrease in the sound speed (Mukhanov, 2005, ch. 9.8). The relative heights of the acoustic peaks is a further diagnostic of the baryon abundance. As seen in Figure 1.2, odd-numbered peaks are higher than even-numbered peaks in a universe with high $\Omega_b h^2$. This is because an increase in the amount of massive baryons reduces the frequency of acoustic oscillations (Dodelson, 2003, ch. 8.7.3). Finally, the power spectrum declines towards higher multipoles (l) due to a process known as "Silk Damping". This damping term is due to imperfections in the photon-baryon coupling, and the characteristic damping scale is influenced by $\Omega_b h^2$ (Durrer, 2008, ch. 4.7).

Through a combination of all the processes listed above, modern CMB observations have been able to place strong constraints on both $\Omega_b h^2$ and $\Omega_m h^2$. Two of the most noteworthy such measurements come from the *Wilkinson Microwave Anisotropy Probe* (WMAP Bennett et al., 2003) and the *Planck* Satellite (Planck Collaboration, 2013a). Different constraints are placed on these parameters depending on what additional data[6] is included in the analysis. We will take the median value (from each paper) of parameters derived through these various means, and we use the systematic variance in the parameters as the uncertainty, if it is larger than the statistical uncertainty listed from the analysis.

From the 9-year data release of WMAP (WMAP9, Hinshaw et al., 2013), we take values $\Omega_b h^2 = 0.02229 \pm 0.00035$ and $\Omega_c h^2 = 0.1138 \pm 0.0032$. From the results paper of Planck (Planck Collaboration, 2013b), we take the values $\Omega_b h^2 = 0.022115 \pm 0.00025$ and $\Omega_c h^2 = 0.11957 \pm 0.0025$. These values allow us to constrain the cosmic baryon

[6] H_0, BAO, Polarization, etc.

fraction as:

$$
\begin{aligned}
\mathrm{f}_b &= \frac{\Omega_b h^2}{\Omega_b h^2 + \Omega_c h^2} \qquad (1.2)\\
&= 0.164 \pm 0.004 \; (WMAP9)\\
&= 0.156 \pm 0.003 \; (Planck)
\end{aligned}
$$

The uncertainty on f_b comes from the propogation of uncertainties on $\Omega_b h^2$ and $\Omega_c h^2$:

$$
\begin{aligned}
\Delta \mathrm{f}_b &= \sqrt{\left(\frac{\partial \mathrm{f}_b}{\partial \Omega_b h^2}\right)^2 \Delta(\Omega_b h^2)^2 + \left(\frac{\partial \mathrm{f}_b}{\partial \Omega_c h^2}\right)^2 \Delta(\Omega_c h^2)^2}\\
&= \sqrt{\left(\frac{\Omega_c h^2 \Delta(\Omega_b h^2)}{(\Omega_b h^2 + \Omega_c h^2)^2}\right)^2 + \left(\frac{\Omega_b h^2 \Delta(\Omega_c h^2)}{(\Omega_b h^2 + \Omega_c h^2)^2}\right)^2}\\
&= \frac{1}{(\Omega_m h^2)^2}\sqrt{\left[\Omega_c h^2 \Delta(\Omega_b h^2)\right]^2 + \left[\Omega_b h^2 \Delta(\Omega_c h^2)\right]^2} \qquad (1.3)
\end{aligned}
$$

It is commonly discussed (e.g., Spergel et al., 2013) that the Planck results yield Ω_m significantly higher and H_0 significantly lower than other previous measurements, including WMAP. This results in the much lower value of f_b as derived from Planck. Earlier estimates (e.g.,WMAP5, Dunkley et al., 2009) placed f_b around 0.17, a canonical value which is often used in the literature. Because of the issues surrounding the interpretation of the Planck data, we will use the WMAP9 measurement of $\mathrm{f}_b \sim 0.164$ for our primary comparisons with low-redshift baryon fractions, although we will attempt to also compare to the Planck constraints whenever possible. One major limitation of this work is the recent uncertainty on the “true” cosmic baryon fraction due to the discrepant results from CMB observations. We hope that subsequent analysis of the WMAP/Planck discrepancies will solve this problem, one way or another.

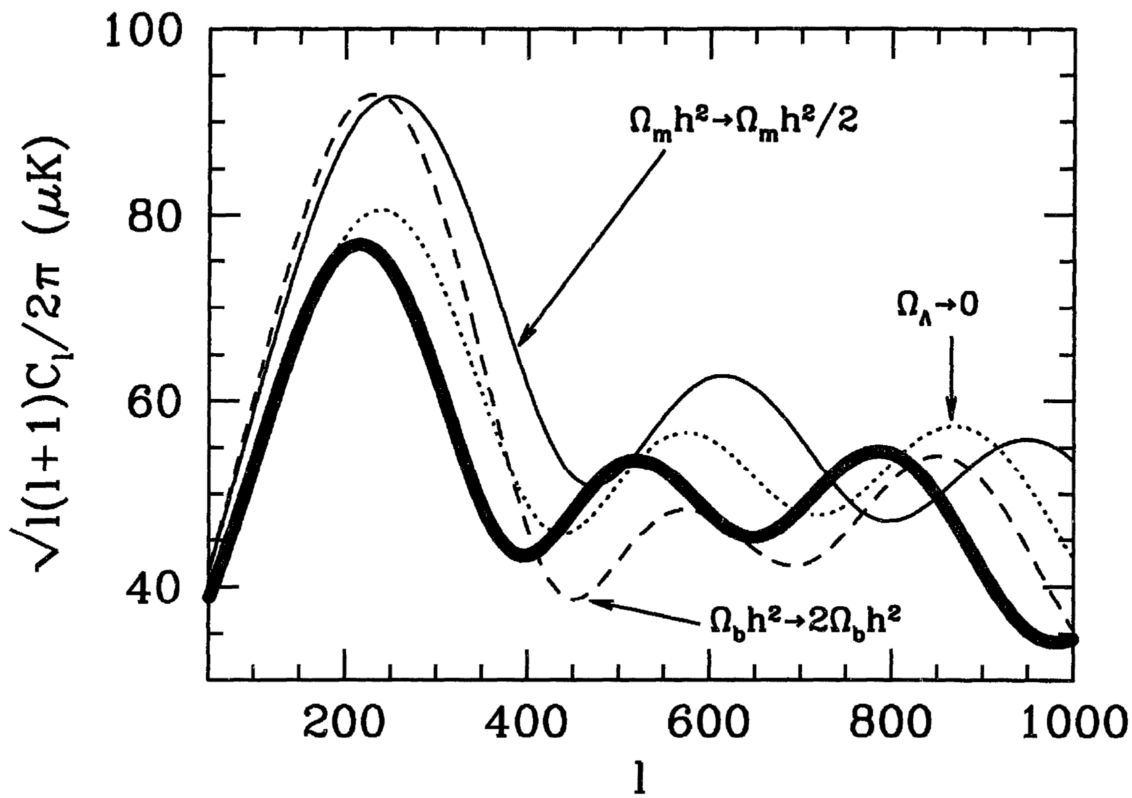

Figure 1.2: The variation in the CMB power spectrum's acoustic peaks due to variations in cosmic abundance parameters. The thick black line represents a fiducial universe with $\Omega_m h^2 = 0.16$, $\Omega_b h^2 = 0.021$, and $\Omega_\Lambda = 0.7$. Other lines represent the results from changes to these parameters, notably an increase in peak height and rightward shift of peaks ($\Delta l > 0$) with an increase in $\Omega_b h^2$. A decrease in $\Omega_m h^2$ has similar (but distinguishable) effects. Figure from Dodelson (2003, Fig. 8.19).

1.2 The Cluster Missing Baryon Problem

Large *galaxy clusters* represent the most massive dark matter halos which have had adequate time to virialize since the big bang. The richest clusters often contain hundreds of large galaxies, while much smaller *groups* may contain several to tens of galaxies. The galaxies are bound to the gravitational well of the combined mass of the cluster, which includes dark matter as well as baryons. Some clusters show a steep pressure profile towards their centers, suggesting that they are dynamically *relaxed* and possess a *cool core* (REFERENCE??). Clusters with flattened central pressure profiles are *disrupted* ???? or *non-cool core* clusters. Because they represent the largest bound objects in the universe, clusters represent one of the best ways of measuring the baryon fraction at low-redshift: they have collapsed from extremely large volumes and therefore are the largest samples of the cosmic dark matter and baryon densities that are not in dramatic dynamical evolution. Additionally, their extremely deep gravitational potential wells are expected to prevent any significant fraction of baryons from escaping the system through feedback effects, such as winds, supernovae, or mergers.

The baryonic component of galaxy clusters is not primarily stored in galaxies, but instead in a hot (kT $\gtrsim$ 1 keV), diffuse gas known as the *Intracluster Medium* (ICM). The ICM can be detected through the X-ray brehmsstrahlung emission of the ionized plasma. X-ray telescopes such as *Chandra*, *ROSAT*, and *XMM-Newton* have been key in detecting the ICM and constraining its distribution and total mass (e.g., Vikhlinin et al., 2006; Eckert et al., 2012). A complementary method of detecting and measuring the intracluster gas is through the thermal Sunyaev-Zeldovich (SZ, Sunyaev & Zeldovich, 1972) effect, wherein the energy spectrum of background CMB photons passing through the cluster is altered, due to reverse-Compton scattering with the charged particles in the plasma.

The stars of individual galaxies make up the remainder of the baryonic mass in clusters. Stellar mass is often derived from the luminosity in starlight, which is converted into mass using typical mass-to-light ratios derived for individual galaxies (Bahcall & Kulier, 2014).

The total mass of clusters is derived through stacked weak-lensing analysis, where the average distortion of background galaxies is measured as a function of cluster-centric radius. These distortions can be inverted to compute the distribution of mass in the cluster which is responsible for the gravitational lensing distortions. Recent weak-lensing analyses (Mandelbaum et al., 2008; Sheldon et al., 2009a) yield accurate constraints on the total mass of clusters, and show that the distribution of mass is fit well by the Navarro-Frenk-White (NFW, Navarro et al., 1996) profile, a prediction from N-body simulations of cold dark matter.

Before addressing the overall masses and sizes of galaxy clusters, it is crucial to outline the definitions for these scales we will use throughout this paper. Because dark matter halos are believed to be self-similar (scaling only by overall mass or central density) their sizes are often given relative to fixed overdensities Δ, the location where the density of matter interior is a particular multiple of the critical density of the universe. For example, $\Delta = 200$ equates to the region in a halo where

$$\rho_m(<r) = \frac{3M(<r)}{4\pi r^3} = 200 \times \rho_{crit}.$$

The mass and radius of a galaxy cluster is typically measured at a characteristic overdensity. For example, many sources in the literature list the cluster mass and radius as M_{500} and r_{500}, measured at an overdensity of $\Delta = 500$. As cluster mass is clustered towards the center, Δ decreases towards larger cluster-centric radii. The gravitational system virializes around $\Delta = 100$ (Eke et al., 1996), so we take the characteristic scales of clusters to be the virial (or halo) mass and radius, $\mathrm{M}_{vir} \equiv \mathrm{M}_{100}$ and $\mathrm{r}_{vir} \equiv \mathrm{r}_{100}$.

Through stacked weak lensing measurements, rich galaxy clusters have been observed to have halo masses of $10^{14} - 10^{15}$ $\mathrm{M}_{\odot}$ (Mandelbaum et al., 2008), and halo radii of around 1 – 3 Mpc (Vikhlinin et al., 2006). Lower-mass "groups" typically have masses around $10^{13} - 10^{14}$ $\mathrm{M}_{\odot}$, and represent the intermediate range between the most massive clusters and large galaxies. The self-similarity of group and cluster halos results in a fairly constant relation between M and r at various overdensities. For example (Rasheed et al., 2011):

$$\mathrm{r}_{vir} \sim 1.3 \times \mathrm{r}_{200} \sim 1.9 \times \mathrm{r}_{500}. \tag{1.4}$$

Using an approximate mass density profile of $\rho_m \propto \mathrm{r}^{-2.5}$, we assume that the total mass scales roughly as $\mathrm{M} \propto \mathrm{r}^{0.5}$, so that

$$\mathrm{M}_{vir} \sim 1.14 \times \mathrm{M}_{200} \sim 1.38 \times \mathrm{M}_{vir}. \tag{1.5}$$

Recent X-ray and SZ measurements have begun to illuminate the hot intracluster plasma, allowing detailed study of these large reservoirs of baryons in groups and clusters. X-ray observations, in particular, are able to directly measure the gas density profile and therefore retrieve the mass. However, because brehmsstrahlung emission declines with the square of the gas density, accurate X-ray measurements have typically been limited to the inner regions of halos. Early studies of this kind in clusters include Vikhlinin et al. (2006, with *Chandra*) and Arnaud et al. (2007, with *XMM-Newton*), while Sun et al. (2009) did similar measurements of the hot gas in groups using *Chandra*. Measuring the gas mass fraction only out to r_{500}, these observations typically found $\mathrm{f}_{gas}(< \mathrm{r}_{500}) \lesssim$ 10–12%, although with large variance between clusters. Importantly, there is a clear trend towards lower gas content in lower-mass halos: nearly all groups and small clusters show gas fractions well below 10% at r_{500}. CITE THE NEW PAPERS WITH MORE GAS FRACTIONS! The stellar fraction in clusters has been observed to increase in smaller halos (Giodini et al., 2009; Bahcall & Kulier, 2014). However, stars make up only a few percent of the total mass even in groups and the smallest clusters, and represent $< 2\%$ of the mass budget within r_{500} in rich clusters: not nearly enough to make up the remainder of the total baryon mass predicted from the cosmic baryon fraction.

These discrepancies have been termed the "Missing Baryon Problem", because observations have not been able to account for the expected abundance of baryons in galaxy clusters. Many attempts have been made to find a solution to this problem through theoretical and computational means. Possibly the most predominant such explanation is that additional energy, non-gravitational energy is injected into the cluster, such as through shocks (Takizawa & Mineshige, 1998), preheating (Bialek et al., 2001), or any number of feedback mechanisms from star formation or AGN activity (Metzler & Evrard, 1994; McCarthy et al., 2007; Bode et al., 2009). The net result of these additional energy sources is to flatten the distribution of hot gas in the ICM, pushing more baryonic matter into the outskirts of the galaxies while leaving the central regions more devoid of gas. These theories predict that more sensitive analysis of the outskirts of groups and clusters ($\gtrsim r_{vir}$) should recover the missing gas mas left unaccounted for by observations of only the inner cluster regions. Additional theories predict that the missing baryons could be residing in additional phases, such as a cool diffuse gas phase, that have yet to be identified observationally (Afshordi et al., 2007; Bonamente et al., 2005).

Is this not enough background on the missing baryon problem? There will be more discussion of these observations and theories in the discussion section. Come back to this section after writing discussion.

Add a representative figure

1.3 The Galaxy-Halo Missing Baryon Problem

Should this be a section or a subsection?

Galaxies form in a range of dark matter halo sizes. Galaxies like the Milky Way and Andromeda (near the high-end of the galaxy mass range) are commonly referred to as L* galaxies, and typically reside in halos with masses upwards of 10^{12} $M_\odot$ (Moster et al., 2010). The virial radii of these systems are around 300 kpc (Werk et al., 2014). The baryonic components which dominate the energy output in these halos (and are therefore the easiest to detect through emission) include the stellar disks, the gas and dust of the interstellar medium (ISM), and a hot, X-ray emitting halo of gas. Yet the most recent estimates of stellar mass in L* galaxies (Behroozi et al., 2010) find that the stellar component makes up only $\sim 5\%$ of the expected baryonic mass, assuming that galactic halos also contain the cosmic baryon fraction. Including the cold ISM gas from HI surveys and the hot X-ray halo (Martin et al., 2010; Gupta et al., 2012, respectively) only increases the estimated baryon fraction in galaxies to around 8%. MORE REFS FROM WERK ON LACK OF BARYONS.

Several models have been developed which attempt to solve this "Galaxy-Halo Missing Baryon Problem". Some predict unseen components in the galactic halo which act as further reservoirs for baryons, but have yet to be accurately measured. These additional components include a highly-photoionized Lyα forest (Sargent et al., 1980; Cen et al., 1994), the warm-hot intergalactic medium (WHIM Cen & Ostriker, 1999; Dave et al., 1999), and a cooler, gaseous phase inside the galactic halos called the circumgalactic medium (CGM Bahcall & Spitzer, 1969; Bergeron, 1985; Lanzetta et al., 1995). Many models predict that galaxies are inefficient at converting gas into stellar mass, and that energetic feedback mechanisms suppress star formation and expel gas from the central galaxy (Somerville & Primack, 1999; Oppenheimer et al., 2010).

Observational studies have begun to probe the CGM in the last few years through studies of QSO or galactic sightlines which pass through the CGM (Steidel et al., 2010; Prochaska et al., 2011; Tumlinson et al., 2011; Werk et al., 2013). When photons emitted by the background quasar or galaxy pass through the CGM, the gas (not energetic enough to be detected in emission) absorbs the characteristic spectral lines from the background spectrum, depending on the chemical makeup of the gas. The most common lines observed in absorption come from neutral hydrogen – hydrogen being the dominant source of baryonic mass in the universe. However, absorption from more highly-ionized species such as CaII (Zhu & Ménard, 2013), MgII, SiII, CII, and OVI (Tumlinson et al., 2011; Werk et al., 2014), while not significant contributors to baryonic mass, can be used to characterize the ionization state of the CGM gas. Knowledge of the ionization state can constrain the total hydrogen mass, including both neutral HI gas in absorption and the ionized HII. The observed metal-line absorption in QSO sightlines and the enrichment of the CGM also suggest that feedback effects are substantial in gaplaxy halos: metals created in the stellar disk are expelled into the outer regions of the halo, or even lost altogether, by feedback winds of $\gtrsim 10^2$ km s^{-1} (D'Odorico & Savaglio, 1991; Chen et al., 2010; Oppenheimer et al., 2012; Booth et al., 2012).

1.4 Our Investigation

In this thesis, we examine the most up-to-date observations available that can help solve the "Missing Baryon Problem", which exists in halos from galactic scales to the most massive clusters. A few previous works (e.g., McGaugh et al., 2010) have studied the problem of missing baryons over many orders of magnitude in halo size, but we present the first comprehensive demonstration that this problem can be solved across nearly all these scales.

The "Cluster Missing Baryon Problem" is primarily a consequence of low observed gas-mass-fractions in the centers of galaxy clusters. Because of the high binding energy of clusters, it is difficult to imagine processes that can completely remove baryons from the cluster potential, and our primary strategy for solving the problem in clusters is to use the most sensitive available observations that constrain the hot gas mass in the outskirts ($r_{500} \lesssim r \lesssim r_{vir}$) of clusters. Gas density profiles in the centers of clusters are shallower than the dark matter (NFW) profile, suggesting that there should be large reservoirs of baryons in the outskirts (e.g., Rasheed et al., 2011). We use published SZ and X-ray observations of cluster outskirts – along with extrapolations of the inner density profiles when necessary – to show that clusters *do contain the expected baryon fraction* in their halos; the baryons are spread further into the outer regions than the dark matter, so that previous observations of only the centers of clusters systematically missed the baryons.

Galaxy halos have significantly lower mass than cluster halos and their binding potential is lower, making it easier to expel baryons from the halo by feedback effects. Because of this, it is possible that the "Galaxy-Halo Missing Baryon Problem" is a consequence of a majority of baryons being removed from the halos altogether. However, the new observations of the CGM allow modernized constraints of the mass-content of the outer galactic halos. We study the problem of missing baryons in galaxies used published absorption measurements of the CGM, which are consistent with the scenario that the *entire baryon fraction* can also be found within the virial radii of galaxies: a large fraction of the baryons simply reside in the hard-to-detect CGM.

Our investigation is organized as follows. In Chapter 2, we present the observations which constrain the baryonic mass within galaxy, group, and cluster halos. We also discuss the ways in which we extract predictions for the baryon fraction at the virial radius from observations of the central regions. In Chapter 3, we show our results and compare the observed baryon fractions in halos to the cosmic baryon fraction derived from BBN and the CMB. We demonstrate that current evidence suggests that there may be no problem of missing baryons in either galaxies or groups and clusters. In Chapter 4, we discuss the implications and limitations of our findings and compare them to simulations. In Chapter 5, we present our conclusions on the subject of the missing baryon problem, and highlight future work that can be done to confirm our findings.

Throughout this paper, we assume a cosmology of $\Omega_m = 0.3$, $\Omega_\Lambda = 0.7$, $\mathrm{H}_0 = 70\,\mathrm{km\ s^{-1}\ Mpc^{-1}}$, when necessary. WHAT OTHER THINGS DO WE NEED TO PREFACE WITH?

Chapter 2

Observations and Data Analysis

2.1 Total Mass in Groups and Clusters

The total mass in groups and clusters can be measured in a number of ways. The most direct method of calculating the mass profile of a large halo is through gravitational lensing of the light of background sources behind the halo. Strong gravitational lensing occurs when the background object (ex: a high-redshift galaxy) is magnified and severely warped by the gravitational potential of the lens (foreground cluster). This allows a very accurate measurement of the mass of the lens, but occurs only rarely when the background/foreground are in a particular alignment. More commonly utilized is the technique of weak gravitational lensing (e.g., Umetsu et al., 2009; Sheldon et al., 2009a; von der Linden et al., 2014), where small distortions of an immense number of background objects are used to statistically determine the mass profile of a foreground halo.

Another common method of estimating the mass of groups and clusters is through the assumption of *hydrostatic equilibrium* (HSE). If the gas in clusters is in HSE, then the pressure gradient offsets the gravitational force:

$$\frac{d\mathrm{P(r)}}{d\mathrm{r}} = -\frac{\mathrm{GM(< r)}\rho(\mathrm{r})}{\mathrm{r}^2}$$

Therefore, assuming the ICM is in hydrostatic equilibrium, the total mass profile can be reconstructed from the observed gas density and pressure profiles:

$$\mathrm{M(< r)} = -\frac{\mathrm{r}^2}{\mathrm{G}\ \rho_{gas}(\mathrm{r})}\frac{d\mathrm{P(< r)}}{d\mathrm{r}}$$

Alternatively, the total mass can be calculated using the density and temperature profiles, assuming the ICM behaves as an ideal gas, P(r)=n(r)kT(r):

$$\mathrm{M(< r)} = -\frac{k\ \mathrm{T(r)\ r}}{\mathrm{G}}\left(\frac{d\log\rho_{gas}(\mathrm{r})}{d\mathrm{r}} + \frac{d\log\mathrm{T(r)}}{d\mathrm{r}}\right)$$

Gas density is typically measured using X-ray observations, as the gas density is easily calculated from the X-ray surface brightness. Temperature can be determined spectroscopically from X-ray observations, and pressure can be measured directly through the thermal SZ effect.

The accuracy of the total mass derived through the assumption of hydrostatic equilibrium (or the "hydrostatic mass") is highly debated, as sources of non-thermal pressure (including cosmic rays, merger-induced shocks, and AGN feedback) can invalidate the assumption of hydrostatic equilibrium. Additionally, deviations from spherical symmetry can bias hydrostatic mass estimates, as many gas measurements are sensitive to the integrated profile along the line-of-sight. Comparing hydrostatic masses to masses derived through weak-lensing analysis can help constrain the bias inherent in the HSE assumption, although weak-lensing masses are also sensitive to the ellipticity of clusters.

The total matter density distribution is often modeled by the NFW profile, an analytical equation first proposed by Navarro et al. (1996) to describe the "universal density profile" of simulated dark matter halos, regardless of size. The NFW profile has the form:

$$\rho_m(\mathrm{r}) = \frac{\delta_c \rho_{crit}}{(\mathrm{r}/\mathrm{r}_s)(1+\mathrm{r}/\mathrm{r}_s)^2} \ .$$

r_s is a characteristic radius representing the central core of the dark matter halo, ρ_{crit} is the critical matter density, and δ_c is a normalization constant which sets the characteristic overdensity of the cluster. Halos which fit the NFW profile are self-similar, in that only r_s is dependent on mass. When $\mathrm{r} \approx \mathrm{r}_s$, the density profile decreases slowly ($\rho_m \propto \mathrm{r}^{-1}$), while at $\mathrm{r} \gg \mathrm{r}_s$ the profile steepens to $\rho_m \propto \mathrm{r}^{-3}$. Observations of group and cluster halos consistently find that the total mass profile follows the NFW profile well (e.g., Vikhlinin et al., 2006; Mandelbaum et al., 2008; Sheldon et al., 2009a; Umetsu et al., 2009).

Several "mass proxies" have been used to estimate the total mass of clusters. Mass proxies are typically easily-observed quantities that are found to correlate strongly with the total cluster mass. Examples include the X-ray temperature ($\mathrm{kT_X} \approx 1 - 10$ keV for groups and clusters), the richness (number of bright galaxies observed within the cluster), and $\mathrm{Y_X} = \mathrm{M}_{gas}\mathrm{T_X}$. Using mass proxies allows observers to place general constraints on the mass of a cluster without requiring deep observations to recover the true gas or mass density profiles. The assumption of hydrostatic equilibrium can also affect the determination of mass through this method, as many Mass-Proxy relations are calibrated against hydrostatic masses of clusters (e.g., Arnaud et al., 2007, 2010).

2.2 Cluster Gas Mass Fraction

The baryonic content of galaxy groups and clusters is dominated by hot gas in the intracluster medium (ICM). Until very recently, the most sensitive X-ray and SZ observations were only able to constrain the gas mass in the ICM in the inner regions of groups and clusters, typically to around r_{500} (e.g., Vikhlinin et al., 2006; Arnaud et al., 2007; Sun et al., 2009). Any more? Because r_{vir} is about twice r_{500}, these observations only probe the inner $\sim \frac{1}{8}$ of the virial volume of group and cluster halos. In order to measure the baryon fraction within groups and clusters, it is essential to consider the gas within a volume substantially larger than that within r_{500}. Here, we describe the relevant observations of groups and clusters which measure both the ICM and total mass to the outskirts of the dark matter halo. Because very few telescopes retain the sensitivity required to measure the gas density in the outskirts of clusters, we also discuss a method of using observed gas density profiles to extrapolate observed gas fractions to higher radii.

2.2.1 Observations

Vikhlinin et al. (2006) derived the gas and total mass profiles of 10 low-redshift (median redshift z= 0.06) relaxed clusters using long-exposure *Chandra* observations. The clusters have a median mass $M_{vir} = 7.3 \times 10^{14}$ $M_\odot$, and range from $M_{vir} = 1.1 \times 10^{14} - 1.5 \times 10^{15}$ $M_\odot$. Temperatures range from kT = 2 − 9 keV. The authors measured X-ray temperature and surface brightness profiles to approximately r_{500}. They modeled the surface brightness profile (which is proportional to $n_e n_p$) to recover the gas particle density, $\rho_{gas}(r)$. The total mass (M_{500}) was derived by solving the equation of hydrostatic equilibrium, using the observed density and temperature profiles, and is well-fit by an NFW profile in most cases. The integrated gas density and total mass profiles were used to derive the gas fraction interior to r_{500}, $f_{gas}(< r_{500})$. This gas fraction ranges widely from cluster to cluster, from 6% to 14%, with median 11%. These observations were also used to derive a useful scaling relation between M_{500} and the X-ray temperature T:

$$M_{500} = (2.97 \pm 0.15) \times 10^{14}\ M_\odot\ h_{70}^{-1} \left(\frac{T}{5\ \mathrm{keV}}\right)^{1.58\pm0.11} . \qquad (2.1)$$

Arnaud et al. (2007) used very similar methods to derive the gas and total mass profiles of 10 low-redshift (median redshift z= 0.09) relaxed clusters from *XMM-Newton* observations. The clusters range in mass from $M_{vir} = 1.2 \times 10^{14} - 1.16 \times 10^{15}$ $M_\odot$, with a median of 4.2×10^{14} $M_\odot$, and temperatures vary from kT = 2 – 8 keV. The total mass also relies on the assumption of hydrostatic equilibrium, and was extrapolated from $\sim r_{700}$ to r_{500} using an NFW profile. f_{gas} was derived out to r_{500} for these clusters, varying from 5.5% to 16%, with median 11%, similar to the Vikhlinin et al. (2006) measurements.

Sun et al. (2009) analyzed the gas fraction in 43 groups from archival *Chandra* observations. All the groups are at low redshifts ($z \lesssim 0.1$). Of these 43 observations, 11 were sensitive enough to measure the X-ray surface brightness to r_{500}, while an additional 12 measured surface brightness to r_{1000} and were extrapolated to r_{500}. The total mass of the 23 best-measured groups ranges from $M_{vir} = 2.0 \times 10^{13} - 2.1 \times 10^{14}$ $M_\odot$, with a median of 1.1×10^{14} $M_\odot$, and ICM temperatures range from kT = 0.7 – 2.7keV. The total mass (assuming hydrostatic equilibrium) and gas mass were calculated using similar principles to Vikhlinin et al. (2006), with errors estimated by using 1000 artificial profiles generated from Monte-Carlo simulations. $f_{gas}(< r_{500})$ for these 23 groups ranges from 5% – 11%, with a median of 8%, lower than for the more massive clusters of Vikhlinin et al. (2006) and Arnaud et al. (2007).

The above three samples were combined in the analysis of **Giodini et al. (2009)** (G09), which used all 10 clusters from Vikhlinin et al. (2006), all 10 clusters from Arnaud et al. (2007), and 21 of the 23 best-measured groups from Sun et al. (2009) to study the group/cluster gas mass fraction over a wide range of halo masses. The authors bin the 42 groups and clusters logarithmically by mass, highlighting that lower mass halos have significantly lower gas fractions. The best-fit trend is:

$$f_{gas}(< r_{500}) = (9.3 \pm 0.2) \times 10^{-2}\ h_{70}^{-3/2}\ \left(\frac{M_{500}}{2 \times 10^{14} M_\odot}\right)^{0.21 \pm 0.03}. \qquad (2.2)$$

Figure 2.1 shows the distribution of the observed gas fractions, as a function of halo mass, measured by the three works above. We will use the G09 bins as 5 independent samples of f_{gas} for different masses.

Recent results from the *Planck* satellite detect the ICM using the Thermal SZ effect, which measures the integrated line-of-sight gas pressure. **Planck Collaboration (2013d)** (PC13) derives a stacked pressure profile for 62 massive clusters which have archival observations by *XMM-Newton*. The cluster sample (detailed in Planck Collaboration, 2011) includes clusters of mass $M_{vir} = 3.3 \times 10^{14} - 2.7 \times 10^{15}$ $M_\odot$, with median mass approximately $M_{vir} = 8.70 \times 10^{14}$ $M_\odot$. X-ray temperatures range from $kT = 3.4 - 13$keV. Total mass (M_{500}) was derived from a scaling relation with the quantity $Y_X = M_{gas}T_X$, an easily-observable quantity that has been found to be a good mass proxy. The scaling relation in question (Arnaud et al., 2010) was calibrated against X-ray derived hydrostatic masses, and so the total mass profile of the stacked *Planck* clusters assumes hydrostatic equilibrium. The total mass beyond r_{500} was calculated assuming an NFW profile. The stacked pressure profile is measured to unprecedented scales ($3r_{500} \approx 1.6r_{vir}$), although the X-ray temperature profile measured by *XMM-Newton* only extends to r_{500}, so the authors extrapolated the observed temperature profile to $3r_{500}$ to match the pressure observations.

Assuming the ICM acts as an ideal gas ($P \propto n_e kT$), the authors inverted the pressure and temperature profiles to retrieve the gas density profile and derive $f_{gas}(r)$ out to $3r_{500}$[1]. The reconstruction of the temperature profile was initially flawed, and the correct gas fraction profile was given in a corrigendum, Planck Collaboration (2013c). f_{gas} increases from r_{500} to r_{vir} (as predicted by Rasheed et al., 2011, see 2.2.2), reaching a peak of $\approx 15 \pm 2\%$ at $1.6r_{vir}$.

Eckert et al. (2013a) (E13) combined the stacked pressure profile from Planck Collaboration (2013d) with a stacked X-ray surface-brightness profile that directly

[1]The authors also derive the gas-fraction assuming a conservative case in which the ICM is isothermal beyond r_{500}, resulting in lower f_{gas}.

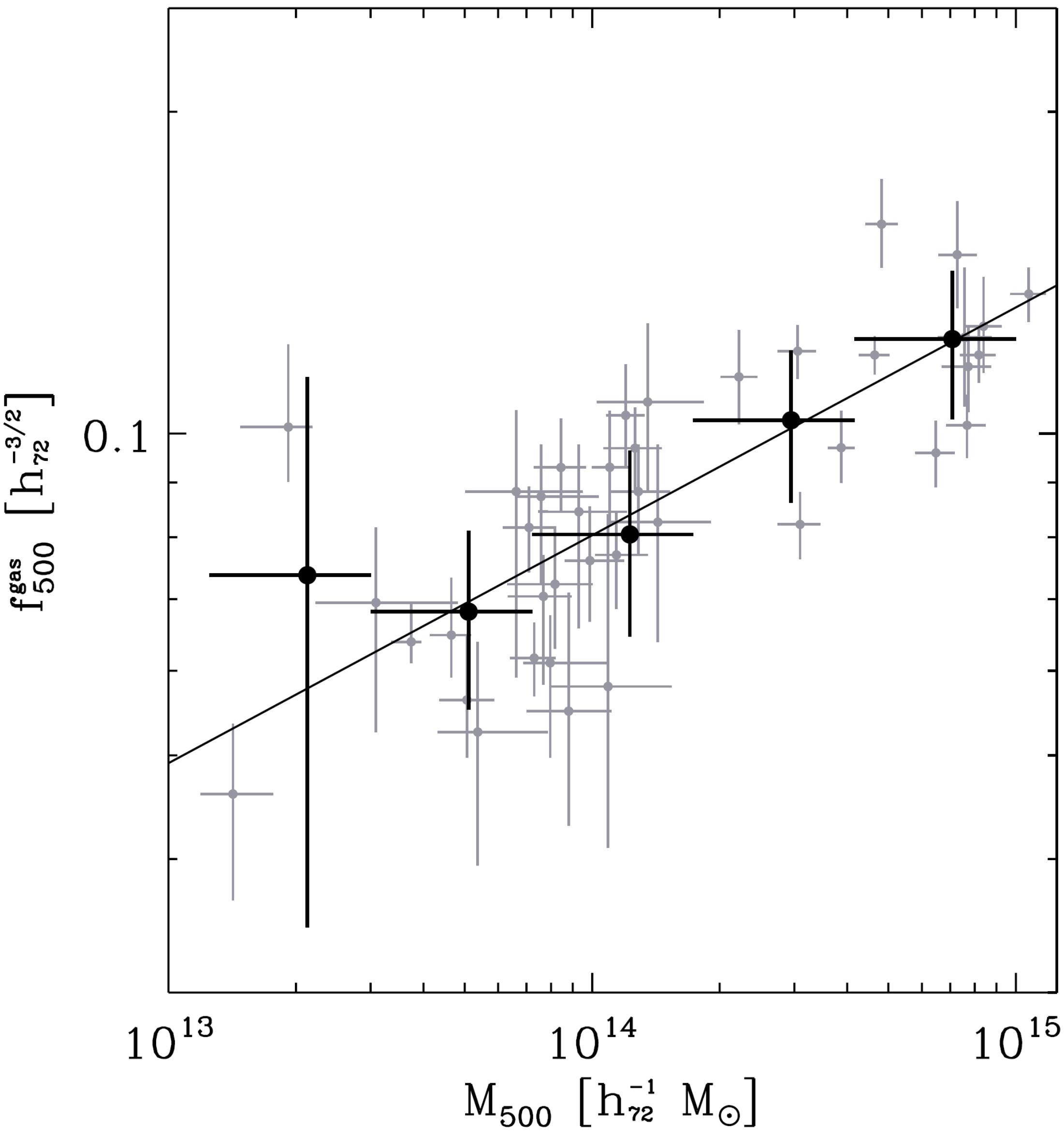

Figure 2.1: The dependence of $f_{gas}(< r_{500})$ on M_{500} ($\sim 0.73M_{vir}$), as presented in Giodini et al. (2009). The light-grey points represent individual group/cluster observations from Vikhlinin et al. (2006), Arnaud et al. (2007), and Sun et al. (2009), while the dark points are the average gas fractions, binned logarithmically with mass. Lower-mass halos show significantly lower gas fractions, with $f_{gas}(< r_{500})$ scaling roughly as ${M_{500}}^{0.21}$.

constrains the gas density to r_{200}. The X-ray observations were performed with *ROSAT*, on a sample of 31 clusters ($z \lesssim 0.2$) of temperatures kT = 2.5 – 9 keV, with median kT = 6.5 keV. The cluster masses range from $M_{vir} \approx 1.4 \times 10^{14}$ to $1.0 \times 10^{15} M_{\odot}$, with median $M_{vir} = 6.0 \times 10^{14} M_{\odot}$[2]. The *Planck* pressure profile, combined with the gas density profile, is used to directly calculate the total mass, assuming hydrostatic equilibrium. This is different from the method used by Planck Collaboration (2013d), which assumed an NFW profile. However, both estimates rely on the assumption of hydrostatic equilibrium either explicitly or implicitly through calibration of the $Y_X - M_{500}$ relation. 18 clusters are in common between the *ROSAT* and *Planck* samples, and the authors separate them into cool-core (CC, 6 clusters) and non-cool core (NCC, 12 clusters) categories. The gas fraction profile is calculated separately for the two categories, and the authors find that NCC clusters have significantly higher gas fractions within r_{200} (0.169 ± 0.010) than relaxed, CC clusters do (0.134 ± 0.011), suggesting that the irregular, non-spherical morphologies of the disturbed clusters may bias the gas fractions high. They also find that f_{gas} increases from r_{500} to r_{200} ($f_{gas}(< r_{500}) \approx 0.12$ for CC clusters).

Umetsu et al. (2009) (U09) observed the ICM of four very massive ($M_{vir} \gtrsim 1 \times 10^{15}$ $M_{\odot}$, kT $\approx 9 - 10$ keV) clusters using Thermal SZ measurements with the *AMiBA* CMB telescope. After deriving pressure profiles from the SZ effect, the authors calculated the gas density profile using archival X-ray temperature measurements and a theoretical temperature-profile (Komatsu & Seljak, 2001). The authors use *Subaru* observations to derive the cluster masses with weak-lensing analysis. The average gas fraction is calculated to the limit of the SZ observations, r_{200}, and is found to be $f_{gas}(< r_{500}) = 0.126 \pm 0.019 \pm 0.016$ within r_{500} and $f_{gas}(< r_{200}) = 0.133 \pm 0.020 \pm 0.018$ within r_{200}. The two uncertainties on each fraction are the statistical error and cluster-to-cluster standard deviation, respectively. These observations also find that f_{gas} in-

[2]The authors do not give the masses of the clusters, so these values are taken from the M-T relation of Vikhlinin et al. (2006) (equation 2.1).

creases with radius beyond r_{500}, in agreement with Planck Collaboration (2013d) and Eckert et al. (2013a). We emphasize that the total mass for these clusters are *not* dependent on the assumption of hydrostatic equilibrium (because they were derived using weak-lensing measurements), so comparisons of f_{gas} from this sample to the same value for samples which assume HSE can put constraints on the validity of the HSE assumption.

Table 2.1 lists the observed data from the samples described above, including the most important characteristics of each sample: median mass (M_{vir}), whether that mass is derived assuming HSE, and the gas fraction at directly-observed radii.

Table 2.1: Samples of Groups/Clusters: Relevant Observations

Reference (1)	**# Clusters** (2)	$\langle M_{vir} \rangle$ ($M_\odot$) (3)	**HSE?** (4)	$f_{gas,500}$ (5)	$f_{gas,200}$ (6)	$f_{gas,vir}$ (7)
G09 Bin 1	2	2.9×10^{13}	$\surd$	0.074 ± 0.028		
Bin 2	7	7.0×10^{13}	$\surd$	0.068 ± 0.005		
Bin 3	17	1.7×10^{14}	$\surd$	0.080 ± 0.003		
Bin 4	5	4.1×10^{14}	$\surd$	0.103 ± 0.008		
Bin 5	10	9.8×10^{14}	$\surd$	0.123 ± 0.007		
PC13	62	8.7×10^{14}	$\surd$	0.125 ± 0.005	0.137 ± 0.003	0.145 ± 0.01
E13 - CC	6	5.9×10^{14}	$\surd$	0.115 ± 0.010	0.134 ± 0.011	
U09	4	7.6×10^{14}		0.126 ± 0.025	0.133 ± 0.027	

(1) G09, PC13, E13, and U09 stand for Giodini et al. (2009), Planck Collaboration (2013d), Eckert et al. (2013a), and Umetsu et al. (2009), respectively. CC represents the sub-sample of cool-core clusters.
(2) The number of clusters in each sample. (3) The median virial mass of the clusters.
(4) $\surd$ marks that the total mass assumes hydrostatic equilibrium.
(5) $f_{gas}(< r_{500})$ (6) $f_{gas}(< r_{200})$ (7) $f_{gas}(< r_{vir})$

2.2.2 Extrapolation of Gas Density Profiles

As seen above, very few observations retain the necessary sensitivity to measure the gas density all the way to r_{vir}. Therefore, to constrain the gas fraction within the entire halo, we can extrapolate the observed gas mass profile (at r_{200} or r_{500}) to higher radius by assuming a power-law profile:

$$\rho_{gas}(\mathrm{r}) \propto \mathrm{r}^{-\alpha_g},$$

where α_g is the slope of the gas density profile, which can in general change as radius increases. The total matter density can be similarly modeled,

$$\rho_m(\mathrm{r}) \propto (r)^{-\alpha_m},$$

with α_m the slope of the total mass density profile. At large radii, the full equation for the gas fraction simplifies to approximately:

$$\begin{aligned} \mathrm{f}_{gas}(<\mathrm{r}) = \frac{\mathrm{M}_{gas}}{\mathrm{M}_{tot}} &= \frac{\int_0^r 4\pi r'^2 dr' \rho_{gas}(\mathrm{r}')}{\int_0^r 4\pi r'^2 dr' \rho_m(\mathrm{r}')} \\ &\approx \frac{\rho_{gas}(\mathrm{r})}{\rho_{tot}(\mathrm{r})} \\ &\propto \mathrm{r}^{\alpha_m - \alpha_{tot}}. \end{aligned}$$

Therefore, the gas fraction can be extrapolated to larger radii using the difference in slopes between the gas density and total mass density profiles.

Rasheed et al. (2011) (R11) used this approach to extrapolate the gas fraction of the G09 cluster samples to r_{vir}. X-ray and SZ observations show that the gas density decreases more slowly with radius than the total mass density ($\alpha_m > \alpha_{gas}$), suggesting that the gas fraction should increase when the cluster outskirts are considered. The authors hoped to place constraints on the amount of "missing baryons" within the virial volume of clusters.

R11 used a large survey of the literature to recover X-ray measurements which constrain the gas density slope out to r_{500}. These measurements include observations with *ROSAT*, *Chandra*, *XMM-Newton*, and *Suzaku*, and cover a wide range of cluster masses and temperatures. Averaging over the many observations, the authors find that the gas density slope at r_{500} steepens with more massive clusters, with α_{gas} ranging from $\approx 1.8 \pm 0.2$ for poor clusters (G09 bin 2, $M_{vir} \approx 7 \times 10^{13} M_\odot$) to $\approx 2.3 \pm 0.02$ for the most massive G09 bin ($M_{vir} \approx 9.8 \times 10^{14} M_\odot$).

Compared to the gas density profile, the total density (NFW) profile is significantly steeper in the outer regions of the halo. In the mass range of the G09 groups and clusters, the NFW profile has a slope of $\alpha_m = 2.6$ between r_{500} and r_{200}, and steepens to $\alpha_m = 2.7$ in the region r_{200} to r_{vir}. Therefore, R11 predicted that the gas fraction rises significantly above r_{500}. Because α_{gas} increases with cluster mass, the gas fraction is predicted to rise more quickly with radius for groups and poor clusters ($f_{gas} \propto r^{0.8}$ for G09 bin 2) than for rich clusters ($f_{gas} \propto r^{0.3}$ for G09 bin 5). For these two bins, this model predicts increases in f_{gas} by a factor of roughly 1.6 and 1.2, respectively, from r_{500} to r_{vir}. This offers an explanation for why the missing baryon problem is more severe in lower-mass clusters: the shallower gas profile implies the ICM is spread farther out in lower-mass halos than in very massive ones.

We adopt R11's extrapolation model in order to approximate the gas fraction at high radius in the samples which do not measure f_{gas} to r_{vir} (all except PC13). α_{gas} for each sample in Table 2.1 is taken from the temperature-slope relation in R11, we do not extrapolate the gas profiles for any individual cluster sample with coverage beyond r_{500}. We assume α_m as above for the NFW profile. We extrapolate f_{gas} from the maximum observed radius, r_a, to a larger radius r_b using:

$$f_{gas}(< r_b) = f_{gas}(< r_a) \left(\frac{r_b}{r_a} \right)^{\alpha_m - \alpha_{gas}} . \tag{2.3}$$

For example, extrapolating the gas fraction of G09's bin 5 from r_{500} to r_{200}:

$$\begin{aligned} f_{gas}(< r_{200}) &= f_{gas}(< r_{500}) \left(\frac{r_{200}}{r_{500}}\right)^{\alpha_m - \alpha_{gas}} \\ &\approx .103\ (1.45)^{2.6-2.3} \\ &\approx .115 \end{aligned}$$

To calculate the uncertainty on the extrapolated gas fraction, we propagate the errors in $f_{gas}(< r_a)$ (or $f_{gas,a}$) and in α_{gas}, assuming no significant uncertainty exists in α_m or r_b/r_a. The fractional errors add in quadrature.

$$\frac{\Delta f_{gas,b}}{f_{gas,b}} = \sqrt{\left(\frac{\Delta f_{gas,a}}{f_{gas,a}}\right)^2 + \left(\frac{\Delta\left(r_b/r_a\right)^{\alpha_m - \alpha_{gas}}}{\left(r_b/r_a\right)^{\alpha_m - \alpha_{gas}}}\right)^2}$$

The uncertainty in the right term is

$$\Delta\left(r_b/r_a\right)^{\alpha_m - \alpha_{gas}} = \left(r_b/r_a\right)^{\alpha_m - \alpha_{gas}} \ln\left(r_b/r_a\right) \Delta\alpha_{gas}\ ,$$

yielding the final result:

$$\frac{\Delta f_{gas,b}}{f_{gas,b}} = \sqrt{\left(\frac{\Delta f_{gas,a}}{f_{gas,a}}\right)^2 + \left(\ln\left(r_b/r_a\right) \Delta\alpha_{gas}\right)^2} \tag{2.4}$$

The gas density profile is expected to steepen at very large radii, such that it eventually matches the NFW profile (e.g., Umetsu et al., 2009), which translates to the gas fraction asymptotically approaching a constant value. At large enough radius, extrapolation of the gas fraction as described above will, therefore, become invalid, as α_{gas} will not remain fixed. The range at which the gas density steepens significantly is not known, however, as observational data does not currently constrain α_{gas} far beyond r_{500}. R11's assumption that this slope remains constant to r_{vir} is therefore a questionable one, but no simple alternatives exist. We also assume α_{gas} remains constant to r_{vir} (and slightly beyond), and emphasize that the our calculation of the gas fraction will be biased high if the gas density slope steepens significantly beyond r_{500}. In Chapter 3, we discuss how our results may be able to constrain the evolution of this density slope.

2.3 Cluster Stellar Mass Fraction

The integrated stellar mass of groups and clusters is also an important (although subdominant) reservoir of baryons in these large halos. The stellar mass of clusters comes almost entirely from the stellar content of the individual cluster galaxies.

G09 approximated the stellar content of a large number (> 90) groups and clusters from the COSMOS survey. Using optical and infrared observations from SUBARU, the authors fit a broad-band spectrum to the detected galaxies in each cluster and used these spectral energy distributions to derive photometric redshifts for the sample. Converting the *Ks*-band (IR) luminosity of detected galaxies to stellar mass, and accounting for the entire predicted galactic mass function, G09 approximated the stellar fraction in clusters of sizes $1 \times 10^{13} - 1 \times 10^{15}$ $M_\odot$. At r_{500}, the stellar fraction was found to be significantly higher ($\approx 6\%$) for groups and poor clusters than for the most massive clusters ($\approx 2\%$). The authors derived a fit to stellar-fraction versus mass of:

$$f_*(< r_{500}) = (5.0 \pm 0.1) \times 10^{-2} \left(\frac{M_{500}}{5 \times 10^{13} M_\odot} \right)^{-0.37 \pm 0.04} .$$

This suggested another possible solution to the increased amount of missing baryons in low-mass halos: the lower fraction of gas could be offset by a higher fraction of stellar mass. Including both stars and gas, however, G09 concluded that the baryon fraction of low-mass clusters still remained below the cosmic fraction ($\approx 12\%$), as did high-mass clusters ($\approx 14\%$).

The results of an extensive Sloan Digital Sky Survey (SDSS) weak-lensing study of stacked groups and clusters has placed unparalleled constraints on the stellar fraction in clusters. The MaxBCG sample (Sheldon et al., 2009a) contains $> 130,000$ clusters between redshifts $z = 0.1 - 0.3$, was binned by richness and luminosity, and stacked by centering on the brightest cluster galaxy (BCG). The mean weak-lensing profile was detected well into the surrounding large scale structure ($\gtrsim 15 - 20\mathrm{r}_{vir}$), as was the averaged optical surface brightness (Sheldon et al., 2009b), allowing the total mass to light ratio (M/L) to be calculated. Bahcall & Kulier (2014) (BK14) developed a model for the stellar mass to light ratio of individual spiral and elliptical galaxies, as well as their relative abundance from the density-morphology relation, and converted the total mass to light ratio into the stellar mass fraction.

Figure 2.2 shows the stellar fraction distributions derived by BK14. The stellar fraction is calculated at r_{200b}[3] as a function of cluster mass. The authors find that the stellar fraction at fixed radius decreases with halo mass, in excellent agreement with G09. The stellar fraction is also calculated as a function of radius, divided into three richness bins, with mass ranges corresponding roughly to $\mathrm{M}_{vir} < 2 \times 10^{13}\mathrm{M}_{\odot}$, $2 \times 10^{13}\mathrm{M}_{\odot} < \mathrm{M}_{vir} < 1 \times 10^{14}\mathrm{M}_{\odot}$, and $1 \times 10^{14}\mathrm{M}_{\odot} < \mathrm{M}_{vir}$. The stellar fraction decreases significantly from the centers of clusters (where the light is dominated by the BCG), asymptotically approaching at high radius a "cosmic" stellar fraction of $\mathrm{f}_{*} \approx 0.01 \pm 0.004$ in all richness bins. The radius at which the stellar fraction reaches this cosmic limit decreases with richness class, suggesting that all clusters contain roughly the same stellar fraction, but that the stellar mass is more widely distributed in low-mass clusters with shallow gravitational potentials.

[3] r_{200b} represents where the density is 200 times the cosmic matter density, not the critical density, and corresponds roughly to our definition of r_{vir}.

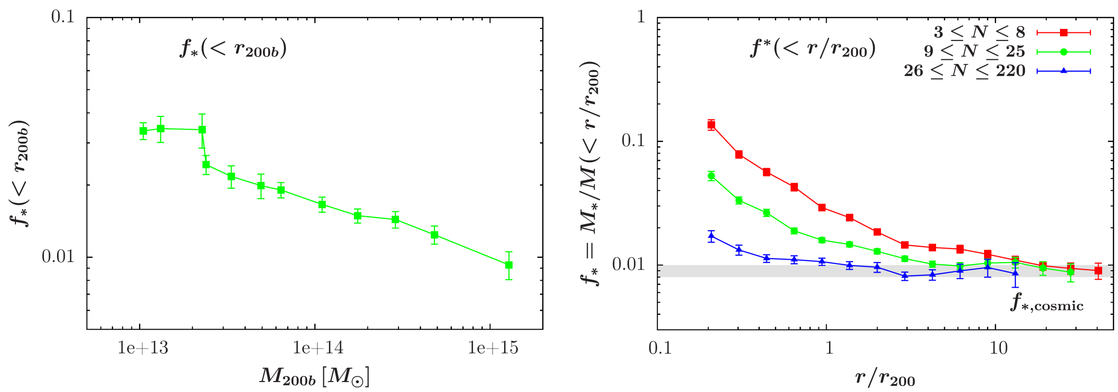

Figure 2.2: The stellar fraction from stacked optical and weak-lensing observations, as presented in Bahcall & Kulier (2014). *Left*: The stellar fraction within $r_{200b} \approx r_{vir}$ in groups and clusters, as a function of total mass. f_* decreases in more massive clusters, in agreement with observations collected by Giodini et al. (2009). *Right*: The stellar fraction as a function of halo-centric radius. The profiles are binned by richness, a proxy for mass. More massive clusters have lower stellar fraction at any given radius (lower-mass halos are more dominated by their BCGs), but the stellar fraction tends towards a constant value at high radius irrespective of mass, the "cosmic stellar fraction" $\approx 1\%$.

2.4 Galaxy Mass Fractions

Studying the distribution of baryons in individual galaxies presents many other challenges not faced in the investigation of clusters. Because galaxy halos are significantly lower mass than cluster halos ($M_{vir} \approx 1 - 2 \times 10^{12} M_\odot$ for a typical L^* galaxy), their gravitational wells are shallower, and it is easier for feedback effects to remove gas from the systems altogether (e.g., Oppenheimer et al., 2010). The lower total mass also translates to a much lower thermal temperature for the gas to be in hydrostatic equilibrium. Therefore, the main diffuse gaseous component of galaxy halos will primarily be too cool and low-density to be detected in emission.

The most obvious and easily detected baryon reservoir in (L^*) galaxy halos is the galactic disk itself, which contains the stellar population and the gas and dust of the ISM. Baryons are also stored in the "circumgalactic medium" (CGM), a large, diffuse region surrounding galaxies, with low temperatures and densities. Observations are beginning, for the first time, to place reasonable constraints on the total mass in this baryonic phase, allowing estimates of the makeup, distribution, and total fraction of baryons in the low-mass halos of galaxies.

2.4.1 The Circumgalactic Medium

The existence of the CGM was first predicted by Bahcall & Spitzer (1969) to explain the presence of absorption features in the spectra of quasars. The emission from quasars was known to come from high redshift, while the absorption lines came from lower redshifts (typically $z = 1 - 3$), had low dispersion velocities, and showed the presence of many abundant elements and ionization states (including absorption from HI, CII, CIV, SiII, and many others). The authors predicted that an extended halo of gas ($r \approx 10^2$ kpc) surrounding normal galaxies ($M \approx 10^{11} - 10^{12}$ $M_\odot$) could produce the observed absorption profiles and dispersion velocities. Even at this early stage, many separate phases of the CGM were predicted, as temperatures ranging from $2 \times 10^4 - 2 \times 10^5$ °K were required to explain the variety of ionization states.

Subsequent observations have confirmed this hypothesis by associating the absorption features in QSO sightlines to nearby foreground galaxies with the expected redshifts. The CGM is a gaseous reservoir in the dark matter halo around galaxies, which extends for several hundred kiloparsecs, and likely as far as the virial radius ($r_{vir} \approx 300$ kpc for an L^* galaxy). The CGM is also likely the major source of pristine gas accreting onto the galactic disk.

The use of QSO and galaxy absorption spectroscopy remains the most powerful tool in statistically characterizing the CGM. The high spatial density of background galaxies and quasars results in a large number of sightlines through the CGM at a wide variety of projected distances. While it is nearly impossible to have enough bright background sources to resolve the distribution of the CGM in any individual galaxy, it is possible to recover the average profile of gas absorption as a function of radius by stacking many sightlines together by their projected distance from the host galaxy.

Steidel et al. (2010) used a sample of 512 galaxy pairs, where both foreground and background galaxies have spectroscopic redshifts and are separated by less than 15" on the sky. At the median redshift of the foreground absorbers ($z \approx 2$), this translates to projected distances within 125 kpc. Absorption profiles (stacked into three projected radius bins) were measured for Lyα, CIV (1549Å), CII (1334Å), SiIV (1393Å), and SiII(1260Åand 1526Å). Hydrogen, the most dominant element by mass in the CGM, is measured in its neutral phase through Lyα absorption, an is observed well beyond 100 kpc. Using an approximate model for populating the CGM by galactic outflows, the authors place a rough constraint on the CGM mass of $M_{CGM} \approx 3 \times 10^{10} M_{\odot}$. By this approximation, the CGM contains roughly the same mass content as the combination of stars and gas in the stellar disk, and amounts to $\approx 3 - 4\%$ of the total mass of the dark matter halo ($\approx 20\%$ of the expected baryonic mass, assuming the halo contains the entire cosmic baryon fraction).

The COS-Halos survey (Tumlinson et al., 2011) was designed specifically to study the CGM in low-redshift galaxies. It uses far-UV spectroscopy of background quasars behind 44 roughly L^* galaxies, observed with the Cosmic Origins Spectrograph instrument on the Hubble Space Telescope. Measuring the column density in Lyα, early results (Thom et al., 2012; Werk et al., 2013) placed a very conservative lower limit on the CGM gas mass of $M_{CGM} > 10^9 M_{\odot}$. Later analysis by **Werk et al. (2014)** (W14) developed a model for the ionization state of the CGM, constrained by the observed absorption of low, intermediate, and high-ionization transitions in metals. This model – which indicates that the hydrogen in the CGM is increasingly ionized at higher radii – is used to greatly improve the limits on the CGM mass. Integrating their best-fit gas density profile to the virial radius (300 kpc), they find that the cool phase ($T \approx 10^4 - 10^5$ K) of the CGM in L^* galaxies has a mass of $M_{CGM} \approx 9.5 \times 10^{10}\ M_{\odot}$. This CGM mass is consistent with the rough estimate made by Steidel et al. (2010), and is similar to the combined mass of the stellar disk and ISM. The uncertainty in M_{CGM} is dominated by saturation in the HI absorption profiles. The minimum CGM mass is $M_{CGM} > 6.5 \times 10^{10} M_\odot$, and could range as high as $M_{CGM} \approx 1.2 \times 10^{11} M_\odot$ if all saturated column densities are 3 times higher than their lower limits. The total halo mass of L^* galaxies is approximately $1.6 \times 10^{12} M_\odot$, so the authors conclude the CGM accounts for $25 - 46\%$ of the expected baryonic mass in galaxies ($M_b = f_{b,cosmic} M_{vir} \approx 2.6 \times 10^{11} M_\odot$).

2.4.2 Estimate of The Galactic-Halo Baryon Fraction

Werk et al. (2014) combined their estimate of the cool gas mass in the CGM with observations of other baryonic components of galactic halos to constrain the total baryon fraction currently detected within the virial radius. The median stellar mass of the COS-Halos galaxies is $\langle M_* \rangle = 4 \times 10^{10} M_\odot$, in agreement with abundance matching estimates (Behroozi et al., 2010). The gaseous component of the ISM, observed with HI surveys, can vary from very little (for elliptical galaxies) to of order the stellar mass (McGaugh et al., 2010; Martin et al., 2010). Together, for a star-forming L^* galaxy, the mass of the stellar disk (the normal galactic component) is given as $7 \times 10^{10} M_\odot$. Thus, the disk contributes about $4 - 5\%$ of the total mass of the galactic halo, or about 27% of the expected baryon content.

The presence of high-ionization absorption lines in CGM profiles suggests that a warm CGM component exists. The ionization model derived by W14 to fit the low-ionization transition abundances severely underestimates the column density of OVI. The authors cite halo models which predict a mass of warm CGM of at least $M_{CGM,warm} \gtrsim 10^1 0 M_\odot$ to explain the observed OVI absorption (Peeples et al., 2014). This mass estimate is highly sensitive to the assumed metallicity in the warm CGM phase, and decreasing Z from $Z_\odot$ to $0.1 Z_\odot$ increases the predicted warm CGM mass by a factor of 10. The constraints on the warm CGM fraction thus range from 0.6%

to 6% of the total halo mass, or $4 - 40\%$ of the expected baryon fraction.

X-ray observations hint at the existence of a diffuse X-ray emitting reservoir outside large galaxies. Estimates of the total mass of this X-ray component range from $10^9 - 10^{10}$ $M_\odot$. W14 argues that, by extrapolating the observed mass of $\approx 510^9 M_\odot$, observed within 50 kpc of an L^* galaxy by *ROSAT* (Anderson et al., 2013), to 300 kpc could increase the mass by a factor of $6 - 14$, although the density profile of this X-ray component is unconstrained. W14 adopts the range of $10^9 - 1.4 \times 10^{10} M_\odot$ for the X-ray CGM from this work. This is between $\approx 1\%$ to 5% of the expected baryonic mass, or $< 1\%$ of the total mass budget. Gupta et al. (2012), however, claims that the Milky Way may have a hot, X-ray reservoir with mass as high as $> 10^{11} M_\odot$, based on OVII absorption observed with *XMM-Newton* and emission from the soft X-ray background. If this is true, the X-ray component of the CGM may be substantially larger than observed by Anderson et al. (2013).

Allow us to summarize the above distribution of the expected baryonic mass ($M_b \approx 2.6 \times 10^{11} M_\odot$) in galaxy halos, as outlined in Werk et al. (2014). The gas in the cool CGM has at least 25% and as much as 50% of M_b. The stellar disk contains $\approx 25\%$, depending on the amount of gas in the ISM. The warm CGM contains between 4% and 40%, and the X-ray CGM is thought to hold $1\% - 5\%$. W14 concludes that current observations could be detecting the entire baryon fraction in galactic clusters, with the primary uncertainty resting on the contents of the warm CGM.

To fit a best estimate to the baryon fraction, we take the mean of the lower and upper limits on each component's abundance, with the exception of the stellar-disk component, which we take to be the upper limit of 4.5% from stars and ISM. We take one-half the range on the component limits as the uncertainty, with the results:

$$\begin{aligned} \mathrm{f}_{disk}(<\mathrm{r}_{vir}) &= 0.045 \pm 0.013 \\ \mathrm{f}_{CGM,cool}(<\mathrm{r}_{vir}) &= 0.060 \pm 0.013 \\ \mathrm{f}_{CGM,warm}(<\mathrm{r}_{vir}) &= 0.035 \pm 0.025 \\ \mathrm{f}_{X-ray}(<\mathrm{r}_{vir}) &= 0.005 \pm 0.004 \end{aligned}$$

Summing these components and propagating uncertainties, assuming they are independent, yields our best estimate of the baryon fraction in galactic halos:

$$\mathbf{f_b}(<\mathbf{r}_{vir}) = \mathbf{0.145 \pm 0.03}$$

If the errors are not independent (and add linearly, not in quadrature), the true lower and upper limits on the baryon fraction are 9.5% and 19%, respectively.

Chapter 3

Results

3.1 The Distribution of Gas and Baryons in Groups and Clusters

Using the observations presented in Chapter 2, we have measurements of the gaseous component of the ICM in halos spanning the entire mass range from poor groups to the most massive clusters. In Figure 3.1, we present the gas fraction in these groups and clusters as a function of radius, out to $1.2\mathrm{r}_{vir}$. We using the extrapolation methods described in Section 2.2.2 when necessary for observations which only constrain the gas fraction within r_{500} and r_{200}. The gas fractions of each sample (both observed and extrapolated) are listed in Table 3.1.

The gas fraction increases with radius in all groups and clusters. Comparing to the "expected" gas fraction of $\approx 15.4\%$, which is the difference between the WMAP9 cosmic baryon fraction (16.4%) and the cosmic stellar fraction of BK14 (1%), nearly all groups appear to contain the expected fraction of gas within the virial radius, or slightly beyond. A large portion of the ICM is, therefore, "hidden" in the outskirts of groups and clusters, where earlier observations within r_{500} were not able to probe.

Figure 3.2 shows the halo gas fraction as a function of the virial mass of the halo.

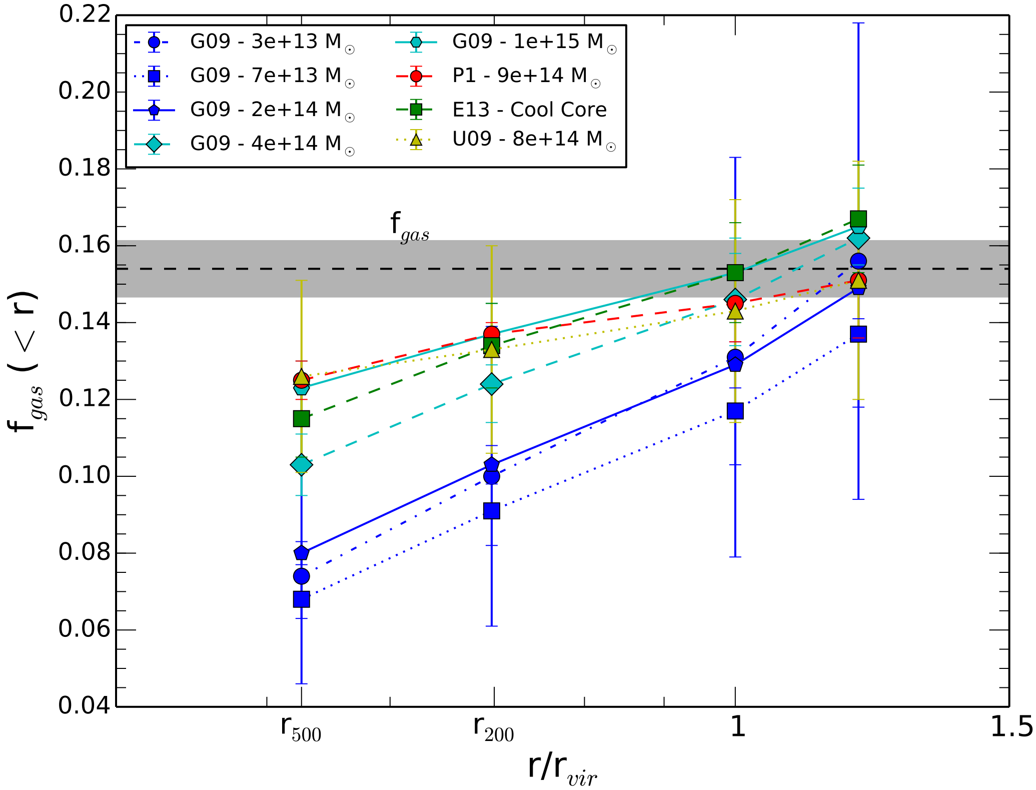

Figure 3.1: The cumulative hot gas fraction for each cluster sample in our study, plotted against the cluster-centric radius. Blue and cyan points (G09) represent data from Giodini et al. (2009), red points (P1) are temperature hypothesis 1 from Planck Collaboration (2013c), green points (E13) from Eckert et al. (2013c), and yellow points (U09) from Umetsu et al. (2009). See Section 2.2.1 for details of these sources. Many observations are extrapolated to $1.2r_{vir}$, as in Rasheed et al. (2011). The f_{gas} line represents the difference between the WMAP9 cosmic baryon fraction and the cosmic stellar fraction from Bahcall & Kulier (2014).

The shortage of gas in low-mass clusters is apparent at r_{500}, with low-mass groups and clusters falling further short of the expected fraction than larger clusters. However, the shallower slope of the gas density profile in low-mass halos leads to a dramatic increase in the gas fraction when extrapolated to higher radius: from r_{500} to r_{vir}, their gas fraction has almost doubled. All halos are consistent with containing the expected gas fraction interior to $\approx 1.2r_{vir}$. Gas may be spread further out than dark matter, with a large fraction residing in the outskirts of groups and clusters, but it

Table 3.1: Gas Fraction in Groups/Clusters: Observed and Extrapolated

Reference (1)	**⟨kT⟩** (2)	α_{gas} (3)	$\mathbf{f}_{gas,500}$ (4)	$\mathbf{f}_{gas,200}$ (5)	$\mathbf{f}_{gas,vir}$ (6)	$\mathbf{f}_{gas,1.2vir}$ (7)
G09 Bin 1	0.93 keV	1.7 ± 0.2	0.074 ± 0.028	0.100 ± 0.039*	0.131 ± 0.052*	0.156 ± 0.062*
Bin 2	1.6 keV	1.8 ± 0.2	0.068 ± 0.005	0.091 ± 0.009*	0.117 ± 0.014*	0.137 ± 0.019*
Bin 3	2.8 keV	1.9 ± 0.07	0.080 ± 0.003	0.103 ± 0.005*	0.129 ± 0.006*	0.149 ± 0.008*
Bin 4	5.0 keV	2.1 ± 0.02	0.103 ± 0.008	0.124 ± 0.010*	0.146 ± 0.012*	0.162 ± 0.013*
Bin 5	8.6 keV	2.3 ± 0.02	0.123 ± 0.007	0.137 ± 0.008*	0.153 ± 0.009*	0.165 ± 0.010*
PC13	†	†	0.125 ± 0.005	0.137 ± 0.003	0.145 ± 0.01	0.151 ± 0.009
E13 - CC	6.25 keV	2.2 ± 0.05	0.115 ± 0.010	0.134 ± 0.011	0.153 ± 0.013*	0.167 ± 0.014*
U09	9.7 keV	2.4 ± 0.1	0.126 ± 0.025	0.133 ± 0.027	0.143 ± 0.029*	0.151 ± 0.031*

(1) Reference abbreviations as in Table 2.1.
(2) The median temperature of the groups/clusters in each sample.
(3) The gas density slope derived from R11.
(4) $f_{gas}(< r_{500})$ (5) $f_{gas}(< r_{200})$ (6) $f_{gas}(< r_{vir})$ (7) $f_{gas}(< 1.2r_{vir})$
*: Value represents extrapolation using the method of Section 2.2.2.
†: No extrapolation required; T and α_{gas} not calculated.

traces the total dark matter mass content closely.

The mass of dark matter halos clearly has an important effect on the distribution of baryons. We therefore combine our samples of groups and clusters into two bins: groups/poor clusters ($M_{vir} < 3 \times 10^{14} M_{\odot}$), and rich clusters ($M_{vir} > 3 \times 10^{14} M_{\odot}$). In Figure 3.3, we show the averaged gas fraction in each bin, as a function of radius. Each point represents the weighted mean of gas fraction at that radius, for all clusters in that mass range. These mass ranges translate roughly to the medium-richness and high-richness bins of BK14, respectively. Therefore, we also include the average stellar fraction, which is measured far beyond r_{vir}.

At r_{500}, the average gas fraction is $\approx$ 7.5% in groups and poor clusters and $\approx$ 12% in rich clusters. The gas fraction increases steeply in groups and poor clusters, reaching about 13% at r_{vir} and 15% at $1.2r_{vir}$. In rich clusters, the gas fraction increases more slowly, reaching 15% at r_{vir}, and 16% at $1.2r_{vir}$. The stellar fraction decreases from 2% at r_{500} to 1.5% at $1.2r_{vir}$ in the low-mass bin, and remains steady at 1% in the high-mass bin. We note that the apparent steepening of the f_{gas} profile at r_{vir} is simply a relic of the logarithmic scale of the X axis.

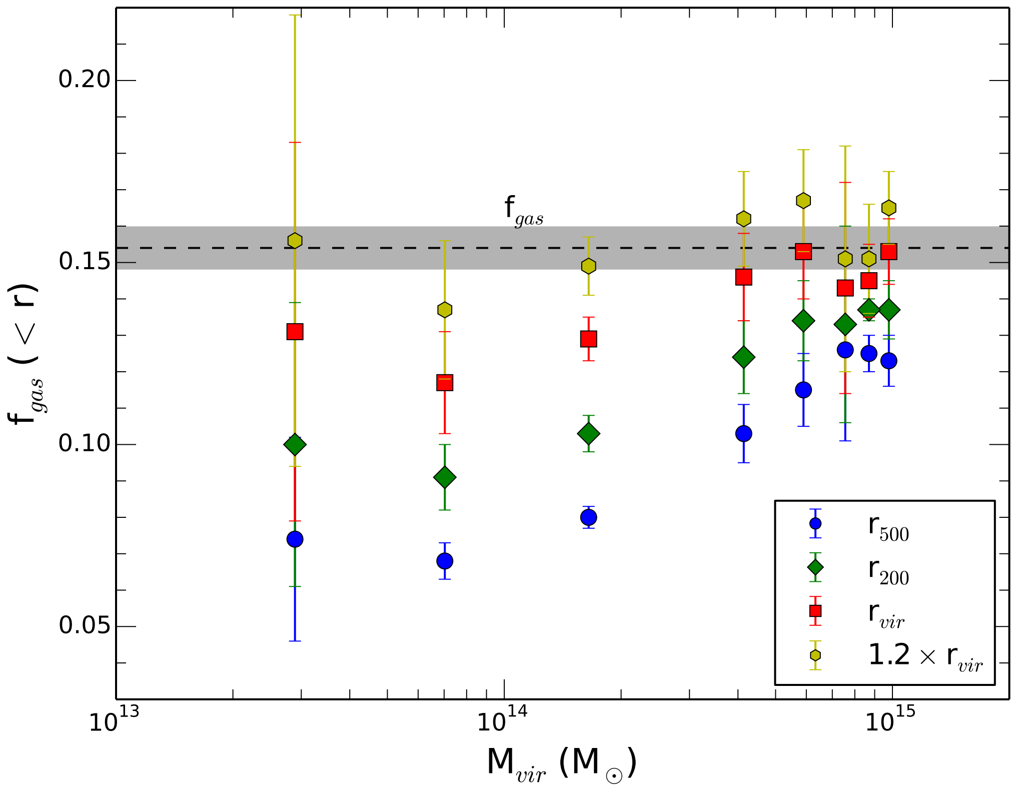

Figure 3.2: The cumulative hot gas fraction for each cluster sample in our study, plotted against the mean halo mass. Blue circles, green diamonds, and red squares show the gas fraction measured at r_{500}, r_{200}, and r_{vir}, respectively. The f_{gas} line represents roughly the expected hot-gas fraction, and is the the difference between the WMAP9 cosmic baryon fraction and the cosmic stellar fraction ($\sim 1\%$, Bahcall & Kulier, 2014).

We are now able to combine the gas fraction and stellar fraction for clusters in these two mass ranges, yielding the total baryon fraction distribution. This is presented in Figure 3.4. We find that the overall baryon fraction increases with radius, reaching the cosmic baryon fraction at $\approx r_{vir}$ in massive clusters and at $\approx 1.2r_{vir}$ in groups and poor clusters. The entire baryonic mass associated with the dark matter of groups and clusters is located within the dark matter halo, indicating that the baryonic matter content of the universe, when considered on large-enough scales, clusters identically to and follows the dark matter mass.

The stellar fraction is observed to approach a constant value at high radii (Bahcall

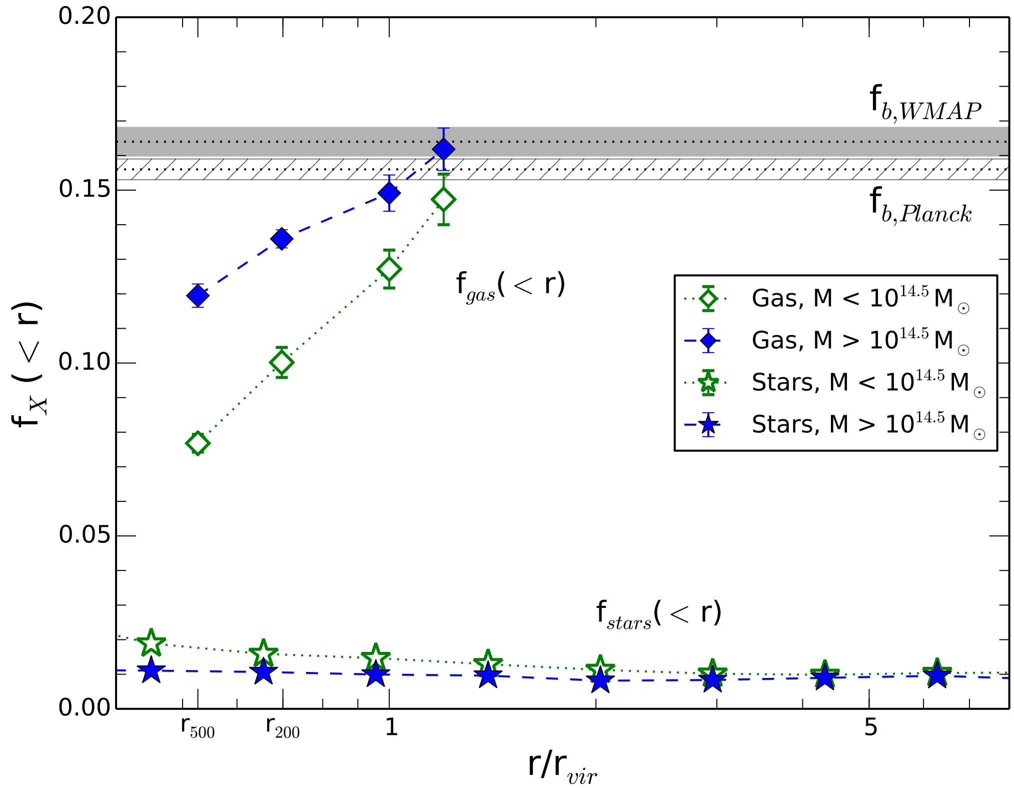

Figure 3.3: The cumulative stellar (Bahcall & Kulier, 2014) and hot gas (Fig. 3.1) fractions for groups and clusters, as a function of cluster-centric radius. Bahcall & Kulier (2014) presented the stellar fraction for various cluster richness bins. The gas fractions of Figure 3.1 have been sorted into corresponding bins, using the mass-richness relation of Sheldon et al. (2009b).

& Kulier, 2014). The gas fraction is predicted to do the same, as the gas density profile likely approaches the total mass (NFW) profile at high radius (e.g., Umetsu et al., 2009, and refs. therein). We approximate this by assuming that, beyond $\approx 1.2r_{vir}$, the gas fraction reaches a constant value, which we represent as an extrapolation of the baryon fraction out to high radius in Figure 3.4. Therefore, current observations are consistent with the picture that the baryon distribution matches the distribution of matter well at all scales larger than the virial radius of clusters.

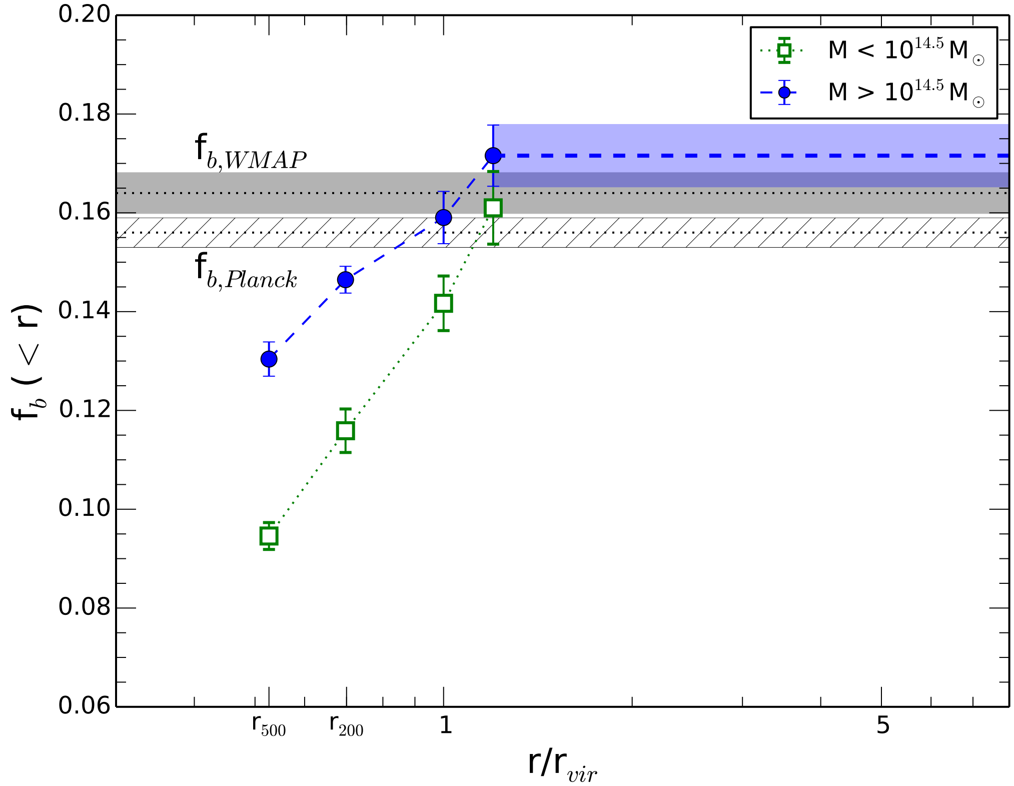

Figure 3.4: The cumulative baryon fraction for groups and clusters, as a function of cluster-centric radius. The baryon fraction (f_b) is the sum of the cumulative stellar fraction and the cumulative hot gas fraction of Figure 3.3. Green squares represent the averaged fractions of groups and smaller clusters, while blue circles represent larger clutsers. The baryon fraction in large clusters appears to approach the cosmic fraction at large scales, and we extrapolate the value at larger scales as the value at $1.2r_{vir}$.

3.2 The Baryonic Content of Halos

We have just shown that, within roughly the virial radius, dark matter halos of both group and cluster sizes are observed to hold the entire cosmic baryon fraction. Combined with the measurements of the baryonic components in galactic halos (Section 2.4.2), we are able to place global constraints on the baryon fraction within halos ranging over three orders of magnitude in mass.

Figure 3.5 presents the combination of these observations on the baryon fraction in halos. Shown, as a function of mass, are the current limits on the baryon fraction for the previously mentioned samples. Observations of the outskirts of groups and clusters show that the baryon fraction reaches the cosmic value between r_{vir} and $1.2r_{vir}$. We plot the baryon fraction for all group and cluster at these two radii, which is the sum of the gas fraction (Figure 3.2) and stellar fraction (Figure 2.2) for clusters of that mass. Observations of galaxy halos show that – between the stellar disk and ISM, cold CGM, warm CGM, and X-ray CGM – the entire baryon fraction could be contained within the virial volume of galaxy halos. We plot the baryon fraction range constrained by Werk et al. (2014), which includes lower and upper limits of $f_b(< r_{vir}) = 9\% - 19\%$. The best-estimate value, taking the mean of the ranges given for each component, is $14.5\% \pm 3\%$.

Groups and poor clusters are still slightly short of baryons within the exact virial radius (shown by red points in Figure 3.5. However, there is no reason to assume that the gas density must cut-off suddenly at this relatively-arbitrary point. Direct observations (Planck Collaboration, 2013d) indicate that the gas fraction in massive clusters continues to increase beyond r_{vir}. Hence groups and poor clusters (where baryons are observed to be more spread-out than in massive clusters) should also have large baryon reservoirs beyond this radius, which justifies our choice to extrapolate f_{gas} to $1.2r_{vir}$.

From galaxies to the most massive clusters, current observations are consistent with the entire baryon fraction being contained within the dark matter halo. Including the baryons out to r_{vir} and slightly beyond, there is no significant shortage of baryons, even in low-mass clusters and galactic halos, where previous estimates claimed a dramatic lack of baryonic mass. While rich clusters tend to have a higher baryon fraction at small-radii, this is not the case outside the virial radius. Considering the entire range of mass, there does not appear to be any strong correlation between enclosed baryon fraction with mass. No matter the scale of the halo, the entire expected baryon mass is bound and contained to this halo. This also suggests that,

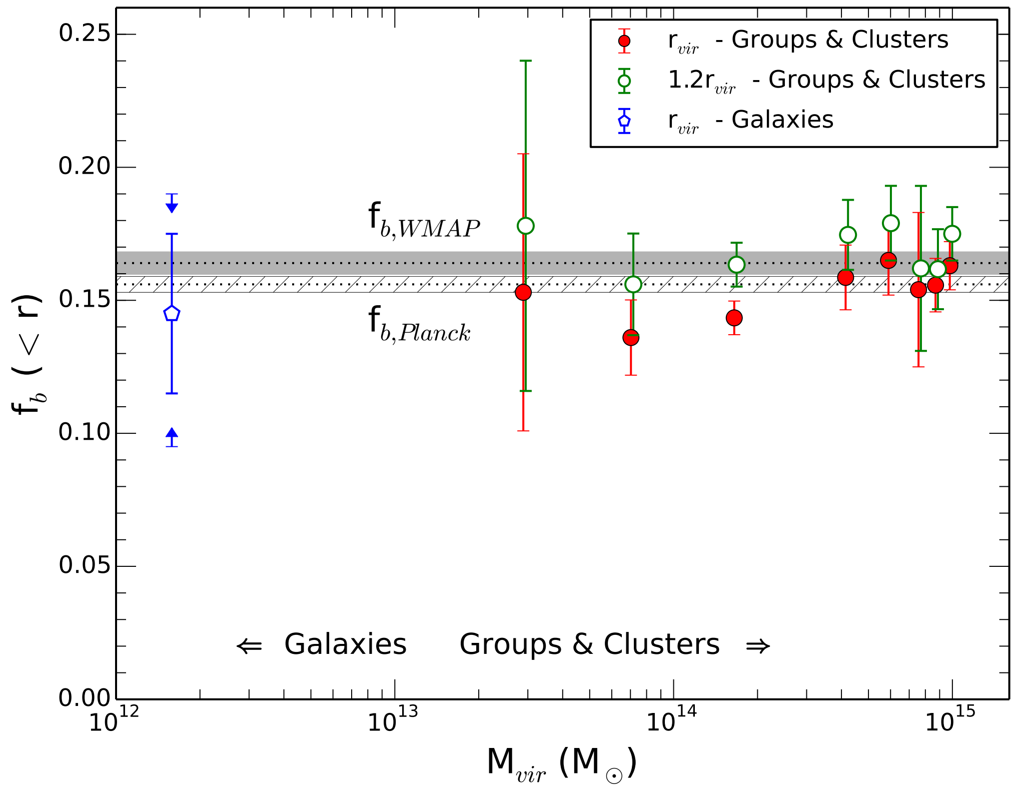

Figure 3.5: The cumulative baryon fraction (f_b) for galaxies, groups, and clusters, as a function of the average mass of the sample. The baryon fraction of groups and clusters (within r_{vir}: filled red points; within $1.2r_{vir}$: open green points) is the sum of the cumulative stellar and hot gas fractions of Figures 2.2 and 3.2. The baryon fraction of L* galaxies (open blue point) is gathered from Werk et al. (2014). The arrows indicate upper and lower-limits on the galaxy baryon fraction, while the error-bars represent the propogated error on the fraction, assuming independent uncertainties on the different galactic components (see text).

in voids and regions with less dark matter, there should be any excess of baryons, as they are not missing from the dense halos. Therefore, in response to the question "Where are the baryons in the universe", we show the answer is: baryons have fallen into and stayed within dark matter halos, and trace closely the total mass distribution in the universe.

Chapter 4

Discussion

4.1 Limitations and Observational Biases

4.1.1 Assumption of Hydrostatic Equilibrium

As was highlighted throughout Chapter 2, there are several different ways to calculate the total mass of group and cluster halos. One key characteristic of a mass estimation method is whether it relies on the assumption of hydrostatic equilibrium. The so-called "hydrostatic mass" (M_{HSE}) can be calculated by combining the gas density profile with either the temperature or pressure profile, a method ubiquitous in X-ray observations. Using mass-scaling relations (such as the Y_{SZ}-M_{500} relation) may also be sensitive to the assumption of HSE if the relation is calibrated against hydrostatic masses. Masses which do not rely on the assumption of HSE are primarily derived from gravitational lensing.

Hydrostatic masses could be systematically biased, relative to the "true" total mass (usually assumed to be the lensing mass, M_{WL}) if there are significant sources of non-thermal pressure in the ICM. These could include kinetic bulk motions or magnetic fields. Hydrostatic equilibrium assumes that the gravitational force (the total mass) is offset by the pressure gradient, so assuming that only the gas pressure contributes can lead to an incorrect calculation of the mass.

The magnitude of the hydrostatic mass bias is of paramount importance to precision cosmology. Cosmological parameters (such as Ω_m) derived from *Planck* cluster counts and hydrostatic mass estimates disagree significantly from values derived directly from the CMB power spectrum, but a large hydrostatic mass bias ($b = 1 - \mathrm{M}_{HSE}/\mathrm{M}_{WL} \approx 0.3$) could relieve the observational tension (Gruen et al., 2013; von der Linden et al., 2014). Such a large bias on the total halo mass would also dramatically affect the gas fraction derived using hydrostatic masses, limiting its use as a cosmological probe (e.g., Grego et al., 2001; Ettori et al., 2009). As the majority of our f_{gas} measurements in clusters were measured relative to hydrostatic masses (with the exception of Umetsu et al. (2009)), our results are likewise sensitive to the hydrostatic bias.

Cosmological simulations are a major tool used to constrain this bias. True mass calculations can be compared to mock X-ray observations which assume hydrostatic equilibrium, determining the bias factor as a function of mass and overdensity. Simulations nearly unanimously indicate that the hydrostatic mass is biased low compared to the true halo mass ($b > 0$) and is more significant towards the outskirts of clusters or in unrelaxed clusters, where merger disruptions and bulk flows become more significant. However, different simulations and physical prescriptions place the bias anywhere from 5% (e.g., Lau et al., 2009; Meneghetti et al., 2010; Burns et al., 2010; Nelson et al., 2012) to 20% (e.g., Arnaud et al., 2007; Nagai et al., 2007; Battaglia et al., 2013).

Observational constraints on the hydrostatic mass bias vary widely. Some weak-lensing measurements of clusters suggest that hydrostatic X-ray or SZ masses are biased low by 10% (Andersson et al., 2011; High et al., 2012), while others indicate this bias is as large as $20 - 30\%$ (Arnaud et al., 2007; Ichikawa et al., 2013; von der Linden et al., 2014). Yet others, however, find no significant difference between weak-lensing masses and hydrostatic masses, with some hints that hydrostatic equilibrium assumptions may even *overestimate* the true mass in lower-mass clusters (Gruen et al., 2013; Israel et al., 2014). Figure 4.1, from Gruen et al. (2013), shows the agreement in measured weak lensing and hydrostatic masses.

The issue of hydrostatic mass bias is far from solved. Due to the inconsistent observational and simulated constraints, it is unclear how large of a hydrostatic correction factor should be included in our measurements of the gas fraction, or if one is even necessary. A bias low in the hydrostatic mass would bias the gas fraction high, meaning that groups and clusters are slightly more deficient of baryons at a given radius. Our reservations to use a hydrostatic correction factor are slightly justified by the fact that one of our samples (U09) measures gas fraction against the weak-lensing mass, and this fraction agrees well with gas fraction derived from the HSE assumption.

4.1.2 Gas Clumping in Cluster Outskirts

The primary means of deriving the gas density profile of clusters is from measurements of X-ray surface-brightness, which scales with the square of electron density. Due to this n^2 dependence, clumpy structures in the ICM will emit more than their share of X-ray, biasing gas density measurements high. The magnitude of this bias depends on the smoothness of the ICM gas distribution, which can vary widely from cluster to cluster.

Simulations typically predict a clumping bias (overestimate of M_{gas}) of $\approx 10-15\%$ (Nagai & Lau, 2011; Battaglia et al., 2013), which increases in unrelaxed clusters and towards cluster outskirts, where recent interactions have a more significant dynamical effect. This could explain the large differences in measured gas fraction between CC and NCC clusters, although observations suggest that the level of clumpiness is overestimated in simulations, and that the average bias is below 10% (Eckert et al.,

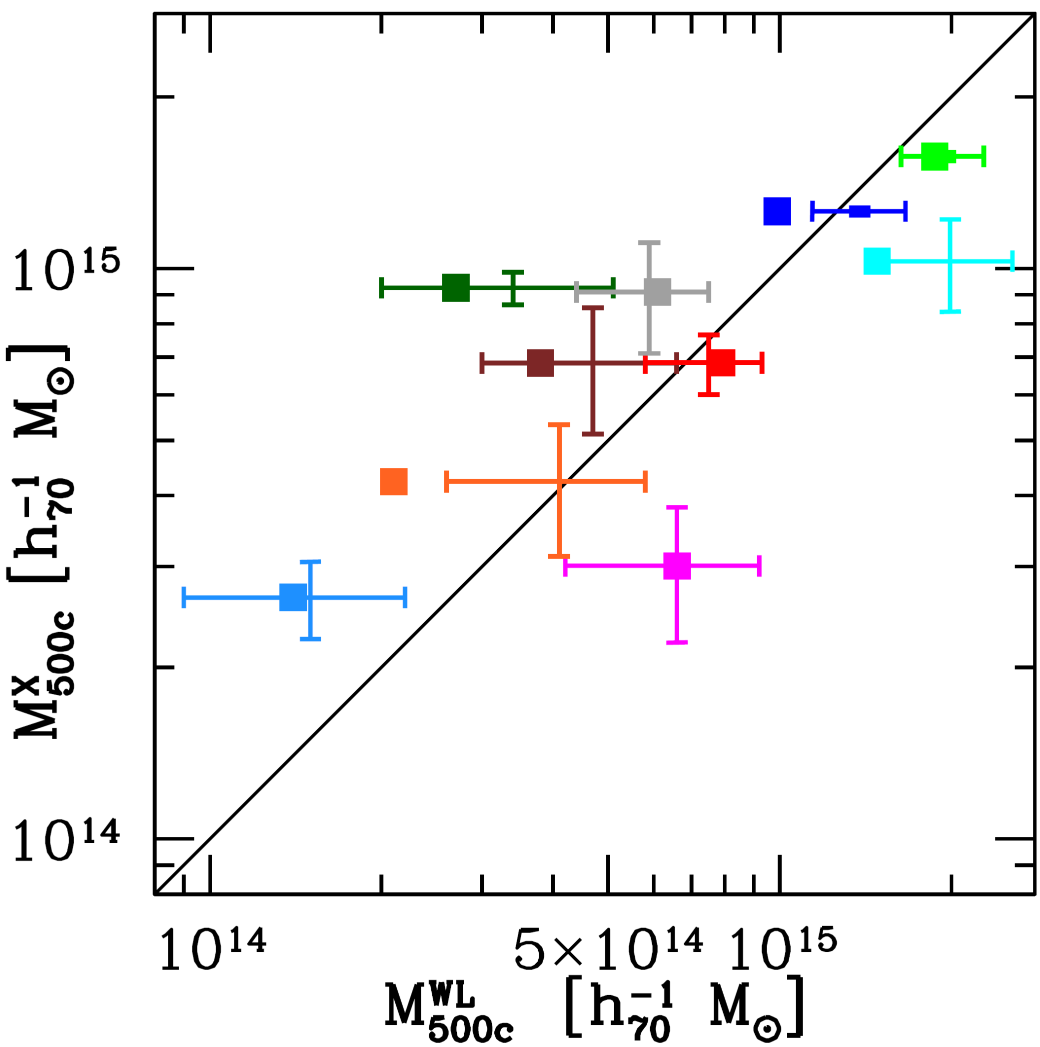

Figure 4.1: A comparison of weak lensing masses (M^{WL}_{500c}) and X-ray hydrostatic masses (M^{X}_{500c}) for SZ clusters, as presented in Gruen et al. (2013). Error bars indicate the best-fit "single-halo" fit, while the filled symbols include corrections to M^{WL} for other structures in the field of view. In tension with simulations, the authors find that hydrostatic masses are not systematically biased low relative to the true cluster mass.

2013b). The majority of our cluster samples represent relaxed (CC) clusters, so we do not include a clumping bias factor at this time. We also note that the P13 (Planck Collaboration, 2013d) and U09 (Umetsu et al., 2009) gas fractions are derived from SZ measurements, which do not suffer from this clumping bias, and agree well with our X-ray data sets.

4.1.3 Extrapolation of the Density Profile Slope

The choice to extrapolate the gas fraction to $1.2r_{vir}$ and then stop is arbitrary. The radius at which the gas profile steepens substantially (α_{gas} increases) is not well constrained. Between r_{500} (where α_{gas} is well measured) and r_{200}, observations disagree whether the slope remains roughly constant (Dai et al., 2010) or steepens by roughly 10% (Ettori & Balestra, 2009). Assuming the true evolution is somewhere in between, the gas density slope should not change appreciably relative to the total mass (NFW) profile, which steepens by about 4% within this range. Therefore, our assumption that α_m and α_{gas} remain constant beyond r_{200} should roughly approximate the increase of f_{gas} with radius.

It is expected that the slope will eventually asymptote to match the total mass (NFW) profile (Umetsu et al., 2009; Battaglia et al., 2013), suggesting that, at large radius, α_{gas} will steepen more quickly that α_m. The point at which this occurs is unknown, but it will taper the growth of f_{gas}, which should eventually reach a constant value, similar to the stellar fraction. Planck Collaboration (2013d) finds that the gas fraction in stacked *Planck* clusters flattens out between 1 and $1.5r_{vir}$. We approximate this by extrapolating f_b as constant above $1.2r_{vir}$. However, until temperature measurements beyond r_{500} improve, the true radius where the baryon fraction reaches a maximum will remain unconstrained.

4.2 Comparison to Simulations

As discussed above, cosmological simulations have been commonly used to examine the magnitude of observational biases on measurements of cluster properties. Here we discuss the measured cluster properties themselves, from the simulations of **Battaglia et al. (2013)**.

The authors conducted a series of smoothed particle hydrodynamic (SPH) simulations with three different physical feedback prescriptions: 1) a "shock-heating" only method, 2) a method that also included radiative cooling and star formation/supernovae feedback, and 3) a prescription including AGN thermal feedback. The simulations produced (at $z = 0$) a sample of over 1000 clusters with $M_{200} > 7 \times 10^{13}$ $M_{\odot}$, and 800 above 10^{14} $M_{\odot}$.

Figure 4.2 shows the cumulative stellar, gas, and baryon fractions in the simulated clusters, as a function of mass (compare to our Figure 3.2). In the shock heating and radiative cooling models, the total baryon fraction within r_{200} is nearly the cosmic value in all clusters ranging from $10^{14} - 10^{15}$ $M_{\odot}$. In the AGN feedback model, f_b decreases in smaller halos, due primarily to suppressed stellar mass production, although partly due to increased non-thermal pressure pushing the gas towards higher radius. These simulations are in good agreement with our results that conclude the entire baryon fraction can be recovered in clusters of all mass ranges.

Figure 4.3 presents the radial distribution of gas, stellar, and baryon fractions for clusters binned by mass. Only the results for the AGN feedback model are presented. The stellar fraction decreases significantly from the center of the clusters, with a higher stellar fraction in low-mass clusters for any given radius. In all mass bins, however, the stellar fraction asymptotically approaches a "cosmic" value of $\approx 10\%$ of the baryon fraction. This behavior matches very well the stellar fraction profile measured by Bahcall & Kulier (2014), although the asymptotic cosmic fraction is higher than observed ($\approx 6\%$).

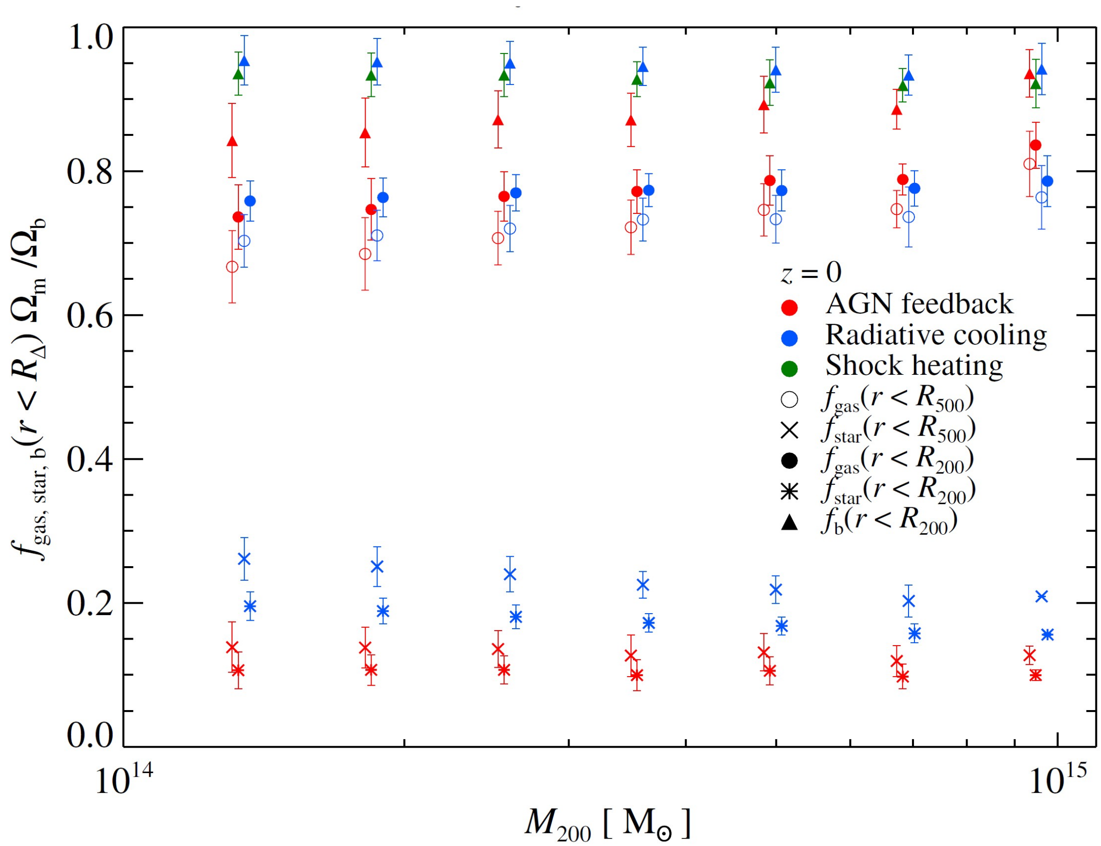

Figure 4.2: The gas, stellar, and baryon fraction (scaled by the cosmic baryon fraction) as a function of cluster mass from a series of simulations by Battaglia et al. (2013). The baryon fraction within r_{200} is close to the cosmic value for the entire mass range of $10^{14} - 10^{15} M_\odot$, except for in the AGN Feedback model, where low-mass clusters have fewer baryons within r_{200}. These simulations are in great agreement with our results, although the simulations predict a large hydrostatic mass bias (Section 4.1.1) that has yet to be confirmed observationally.

The gas fraction profile also matches our observed trends well. The gas fraction in low-mass clusters is significantly lower in the central cluster regions, but increases more rapidly with radius than high-mass clusters. The gas fraction in clusters of all mass converges towards the same profile at high radius. Of particular interest, however, is that even at $r > 3r_{200}$ the gas fraction is still increasing steadily. If this represents the gas profile in real clusters (not certain, as the different feedback models have different behavior in the outskirts), then the our assumption that the gas fraction remains constant above $1.2r_{vir}$ may need adjustment.

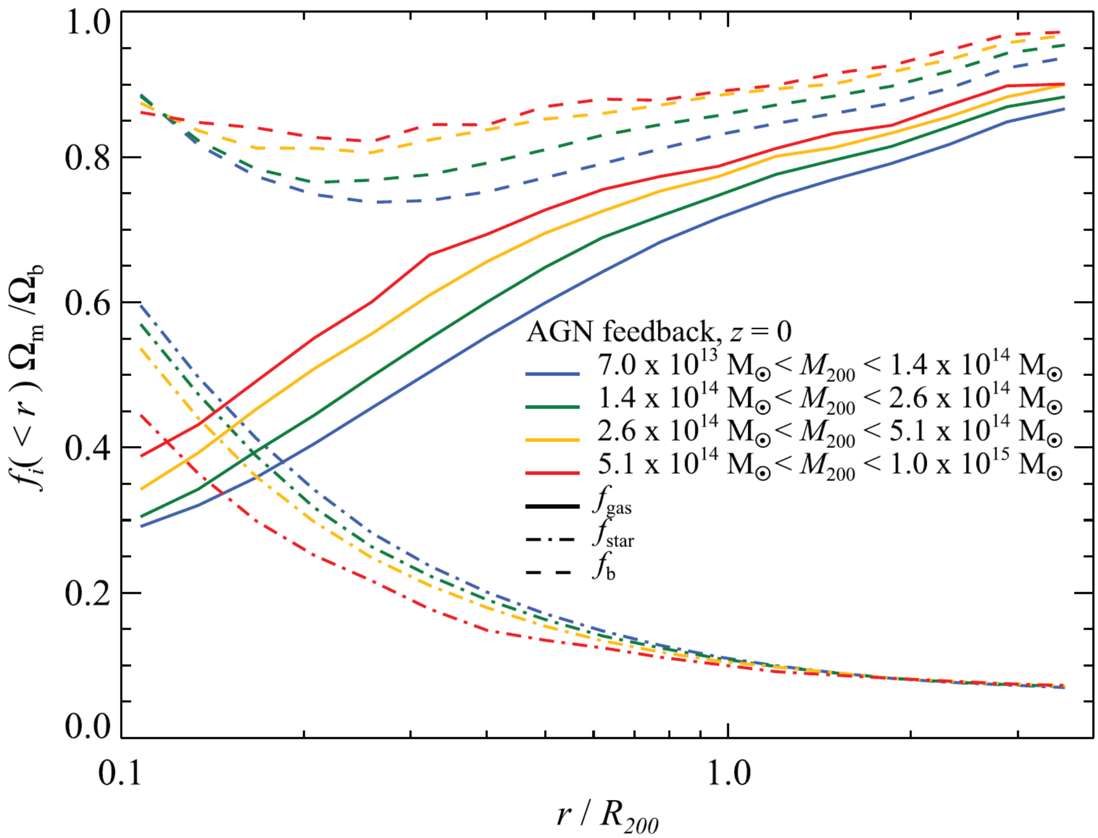

Figure 4.3: The gas, stellar, and baryon fraction distributions (scaled by the cosmic baryon fraction) as a function of radius in the simulations of Battaglia et al. (2013), binned in four parts by cluster mass. The stellar fraction and gas profiles match observations well, and the total baryon fraction approaches the cosmic value at high radius.

The overall baryon fraction increases from a minimum of $70-80\%$ cosmic around $0.5\mathrm{r}_{200}$ to $> 90\%$ outside the virial radius. The fact that the baryon fraction does not reach the cosmic fraction until very high radius ($> 4\mathrm{r}_{200}$) is in slight tension with our results, and improved observations of the gas profile slope beyond r_{200} will help constrain whether these simulations accurately predict how far beyond the virial radius cluster baryons are pushed out. Additionally, the simulations assume a cosmic baryon fraction of $\mathrm{f}_b = 0.172$, higher than current observational estimates. The increased baryon abundance could lead to enhanced feedback effects, pushing baryons further from the cluster centers than actually observed. Simulations which match the current cosmological constraints would help clarify this issue.

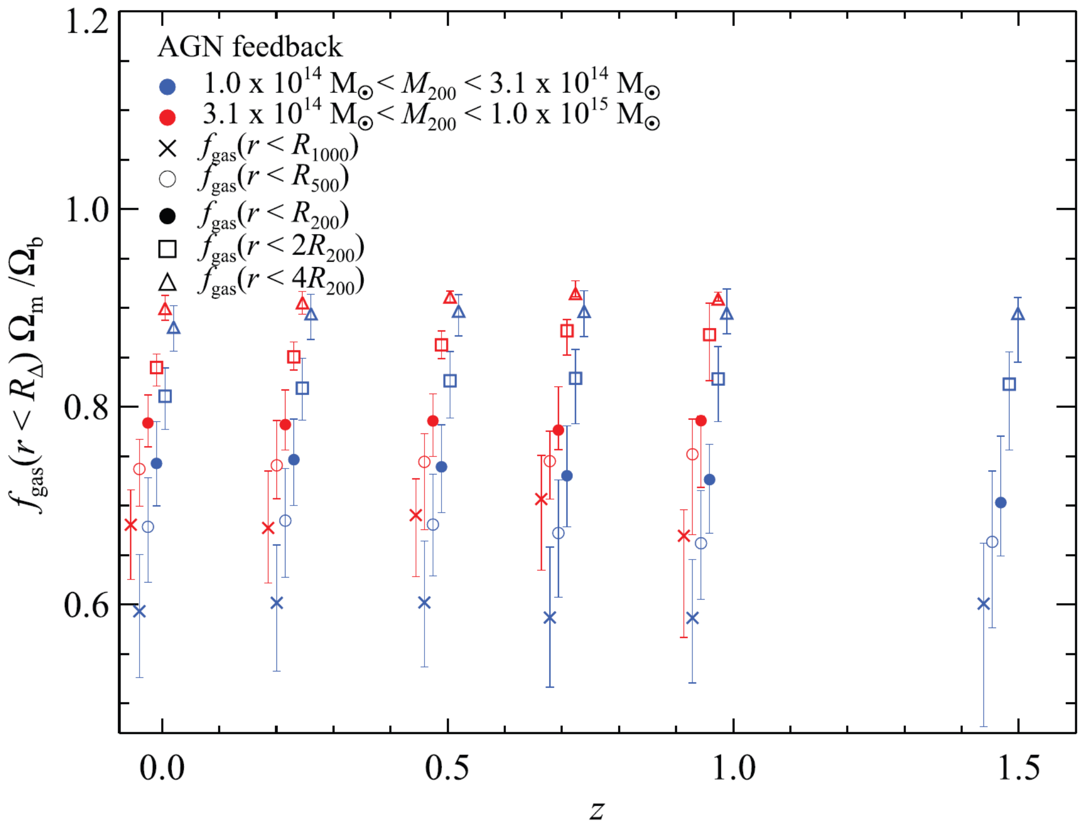

Figure 4.4: The gas fraction (scaled by the cosmic baryon fraction) within various radii, as a function of redshift, as measured by the simulations of Battaglia et al. (2013), and binned by mass. There is no significant redshift evolution of the gas fraction within any given radius, except possibly within $2r_{200}$, suggesting that measurements of the cluster baryon fraction should be fairly redshift independent back to $z \approx 1$, where massive clusters first begin to form.

Finally, in Figure 4.4, we show the redshift evolution of the gas fraction of the Battaglia et al. (2013) simulated clusters. Measured from the cluster centers to far beyond the virial radius, the gas fraction appears constant with redshift at all radii, with the exception of a slight decrease within $2r_{200}$. Measured from $z = 1.5 - 0$, this shows remarkable stability within the ICM over many gigayears, including the phase when the most massive clusters begin to form. WHAT DOES THIS MEAN COSMOLOGICALLY? WHAT ELSE SHOULD WE SAY ABOUT THE REDSHIFT EVOLUTION?

4.3 Implications

4.3.1 Where are the Baryons?

Our results show that the entire expected baryon content of dark matter halos can be detected or inferred using current observations. While the baryonic components (such as stellar mass or ICM gas) are more extended than the dark matter, they are still bound to their host halos, and there is no significant problem of baryons missing from halos. Therefore, the answer to the question, "Where are the baryons in dark matter halos?" is answered simply as: they are all found in the halos, distributed in various combinations between the central regions and the diffuse outskirts.

The size and frequency of virialized halos define the overall structure of matter in the universe. Because baryons populate in equal proportions galactic, group, and cluster halos, on large scales they represent excellent tracers of the overall dark matter distribution and structure. A relevant physical scale seems to be the halo virial radius: this scale separates the regimes where baryons do/do not trace the dark matter. On scales smaller than the virial radius, baryons are under-abundant, relative to their cosmic fraction, and this abundance is dependent on the overall mass of the halo. However, averaging on scales larger than r_{vir}, baryons match the dark matter distribution of the cosmos at a constant, unvarying fraction.

This suggests new ways to place constraints on the cosmology of the universe. Dark matter is notoriously difficult to detect or measure accurately, with the only direct method being weak lensing. Baryons, however, emit or absorb radiation in a variety of measurable ways. The knowledge that baryons trace the underlying dark matter profile allows the use of easily observed baryon mass distributions to constrain the abundance and masses of halos (e.g., Ettori et al., 2009).

Furthermore, our results can help place constraints on the expected contents of baryon reservoirs exterior to halos. Examples of these interhalo components include the IGM, WHIM, and Lyα forest outside of galaxies and clusters, as well as the sparsely populated cosmic voids. If halos were deficient in baryons, then baryons in these interhalo components would necessarily be overabundant, holding the additional baryons removed from halos. Because halos retain their relative baryon fractions, these diffuse components must also, and the baryonic mass in these components (as a whole) must match the total dark matter mass outside of halos in the cosmic fraction. How else should we answer where are the baryons?

4.3.2 Deviations from Self-Similarity

Dark matter halos (both observationally and in simulations) are found to fit the NFW density profile, and hence are, roughly, "self-similar". This means that all dark matter halos have the same proportions and shapes, varying only by overall size. Assuming simple gravitational collapse, physical properties of baryons in clusters (such as pressure and temperature) are likewise to obey "universal profiles", once scaled to the appropriate halo size (e.g., Arnaud et al., 2010; Planck Collaboration, 2013d).

Although we have shown that the entire baryonic mass can be accounted for in halos ranging over three orders of magnitude in mass, the gas and stellar fractions reach their expected cosmic levels at overdensities which appear to be mass-dependent. Pure self-similarity would suggest that, for instance, the stellar fraction should reach the cosmic value of 0.01 at the same overdensity (such as r_{200} or r_{100}) regardless of halo mass. However, observations of the gas fraction (Section 3.1) and the stellar fraction (Bahcall & Kulier, 2014) in clusters indicate that the scale at which these fractions asymptote to the cosmic values decreases with cluster mass. Baryons are spread to larger scales, relative to the halo size, in smaller halos, an observation which is supported by cosmological simulations (Battaglia et al., 2013).

Therefore, baryonic physics plays an important role in shaping the distribution of baryons in dark matter halos. Feedback effects (such as merger shocks, AGN feedback, and star formation) are able to push baryons further into the outskirts of small halos than in large halos, due to the decreased gravitational potential. However, as our results indicate, these feedback effects are not so powerful as to remove a substantial fraction of baryons from the halos altogether, and nearly the entire baryon fraction remains bound to dark matter halos.

4.3.3 The Contribution of Individual Galaxies to Clusters

Bahcall & Kulier (2014) found that the overall mass-to-light ratio of clusters matches closely the average mass-to-light ratio of individual galaxies, when normalized by the changing ratio of elliptical and spiral galaxies with cluster radius (the "density-morphology relation"). This is consistent with the picture that the entire dark matter content of clusters is comprised of the dark matter originally bound to galaxy halos, which fell into the clusters and was stripped to form the cluster halo. There is no reason, they argue, to assume that groups and clusters contain more dark matter (relative to light) than galaxy halos do (e.g., Ostriker et al., 1974; Guo et al., 2010).

Our results suggest a similar interpretation involving the entire baryonic content of clusters. We show that clusters of all sizes contain the cosmic fraction of baryons within about the virial radius, distributed in about 15 parts hot ICM gas to 1 part stellar mass. Yet, combining the stellar mass of galaxies with observations of the multiphase CGM gas, Werk et al. (2014) demonstrates that large, L^* galaxies also contain approximately the cosmic fraction of baryons within their halos. If clusters form entirely from the disruption of infalling galaxies, then the galaxies would bring a baryon abundance equal to the cosmic fraction with them, filling clusters with dark matter, stars, and gas from their halos. Clusters do not necessarily need a separate source of gas to explain the high abundance of baryons in their halos: the cluster baryons could be comprised entirely of the baryonic mass once held in the disk and

CGM of constituent galaxies. The ICM, therefore, could be the stripped remains of galactic ISMs and CGMs, with the stellar disks either remaining as cluster galaxies or being dispersed as the diffuse intracluster light (ICL).

One inconsistency that arises in this model is the stellar makeup of the baryons in structures: around 15% of the baryons in L^* galaxies are held in stars, while the stellar mass of clusters is only $\approx 6\%$ of their total mass. One possible explanation for this discrepancy is a suppression of star formation in the galaxies that fall into clusters. Due to the hot, relatively dense ICM, frictional heating of the ISM of infalling galaxies could prevent these galaxies from forming stars. The stellar fraction in clusters could be explained if galaxies which merged into clusters had ≈ 2.5 times lower stellar mass than presently observed field galaxies, leaving the remainder of the baryons in a gaseous phase to populate the ICM. This level of star formation suppression is high, but not unreasonable. Most large clusters collapsed around redshift $z = 1 - 1.5$ (Eke et al., 1996; Battaglia et al., 2013) and while the galactic star formation rate (per year) peaked around $z = 2-3$, a large majority of stellar mass formed during the long period between $z = 2 - 0$ (Hopkins & Beacom, 2006). Even if star formation suppression of this magnitude did not occur, we can place a lower limit on the total contribution by galaxies to the baryons (and dark matter) of clusters using the observed ratio of stellar fraction.

In the conservative case, let us assume that the entire stellar mass of galaxies formed during the peak of star formation, such that galaxies are not forming any stars during the period of cluster growth, and that there is no inherent difference between galaxies which will fall into clusters and those that will not. Therefore, the current observed stellar fractions of field galaxies (15%) represents accurately the stellar fraction of cluster galaxies just before they merge, and no star formation suppression effects need to be considered. Assuming no star formation occurs except in galaxies, then the total stellar fraction in clusters (6%) came entirely from the previously formed stars of merging galaxies. Galaxies, therefore, must have contributed $6/15 = 40\%$ of the total mass of clusters, with the remaining 60% coming from diffuse IGM gas which collapsed into the cluster along with the galaxies.

This estimate represents a lower limit, due to the assumption of no star formation past $z \approx 2$. In reality, stellar mass buildup has continued strongly to $z = 0$, such that galaxies which began merging into clusters at $z \approx 1$ likely had a stellar fraction lower than 15%. In this case, star formation in cluster galaxies will surely be suppressed by falling into clusters, raising our estimate of the galactic contribution to clusters.

According to the models of Hopkins & Beacom (2006), the accumulated stellar mass in galaxies at $z = 1$ was only $\approx 60\%$ its current value, and only 45% at $z = 1.5$. If galaxies had a 50% overall suppression in star formation after falling into clusters at $z = 1.5$, their current stellar fraction would be 11%, suggesting that individual galaxies contributed $> 50\%$ of the matter of clusters, while suppression of 80% of star formation would raise the galactic contribution to clusters to 70%. CITE BAHCALL,BAHCALL,POP ON THE STRIPPING OF GAS IN GALAXIES FALLING INTO CLUSTERS??

Chapter 5

Summary and Conclusions

In this thesis, we present a synthesis of observational constraints on the distribution and abundance of baryons in dark matter halos over a wide range of sizes. Baryons, while only 16% of the total mass in the universe, are the most easily detectable form of matter and are incredibly important tools in understanding and observing the formation of structure and dark matter halos in the universe. Previous observations suggest halos are deficient in baryons relative to the cosmic fraction, a discrepancy known as the "Missing Baryon Problem". We trace the baryon distribution in halos from galactic scales ($\mathrm{M}_{vir} = 10^{12}\mathrm{M}_{\odot}$) to groups ($\mathrm{M}_{vir} = 10^{13}\mathrm{M}_{\odot}$), and clusters ($\mathrm{M}_{vir} = 10^{14} - 10^{15}\mathrm{M}_{\odot}$) to address the missing baryon problem and to obtain a global picture of the distribution of baryons relative to dark matter in the universe.

Our group and cluster gas mass data is comprised of a collection of X-ray and SZ measurements of the gas density, temperature, and pressure profiles in the ICM. The total mass is derived either through the assumption of HSE or by using weak lensing. When the gas fraction is not measured to the virial radius, we extrapolated the observed gas fraction using gas density profile slopes appropriate to the given halo mass or ICM temperature. Our galaxy cluster data comes from a compilation by Werk et al. (2014), and includes absorption measurements of the multiphase CGM, stellar masses, and ISM masses from HI surveys.

Our main results are as follows:

1. Although the gas fraction within r_{500} in clusters is significantly lower than the cosmic baryon fraction, the gas density profile has a shallower slope than the total mass (NFW) profile, resulting in an increasing gas fraction at higher radius.

2. The gaseous ICM is more extended in low-mass halos, explaining why the gas fraction is observed to be low within r_{500} in these halos. The gas density slope in groups and poor clusters is shallower than in massive clusters, and our extrapolations predict that the gas fraction of all groups and clusters should converge to the cosmic value near r_{vir}.

3. The cluster stellar fraction at any given radius is higher in groups and poor clusters, although in clusters of all sizes the fraction asymptotically approaches the "cosmic" stellar fraction 0.01 ± 0.004 at high enough radius.

4. Observational constraints on the gas content of galactic halos find the cool CGM can account for $25-50\%$ of the total baryonic mass. Current constraints of the stellar disk, ISM, and multiphase CGM are consistent with the galactic baryon fraction matching the cosmic value within the viral radius.

5. Combining the observed baryonic components of galaxy, group, and cluster halos, we show that dark matter halos contain the cosmic fraction of baryons within approximately the virial radius, across three orders of magnitude in halo mass.

6. The baryon distribution of the universe traces the dark matter distribution well, with no need for additional unseen or unbound reservoirs of baryons from halos. Averaged over scales larger than the virial radius, baryons map the total

structure of the universe, and the baryonic mass of clusters is an effective proxy for the total mass.

7. The baryonic content of halos is not self-similar. Baryons in less-massive halos are pushed farther into the outskirts by feedback mechanisms and shallow gravitational potentials, not reaching the cosmic fraction until higher radii. The abundance of different baryonic components (particularly stellar mass and gas) also changes with cluster mass.

8. The consistent baryon fraction in galactic and cluster halos suggests that cluster dark matter and baryonic masses could be composed entirely of matter originally in galactic halos which fell into cluster halos. Using the ratio of stellar fractions, we show that galactic halos contribute **no less than** 40% of the total matter of clusters.

Improvements on the precision of our results will come from better constraints of the ICM temperature profile at high radius (in clusters) and of the mass in the warm CGM phase (in galaxies). Additionally, further weak lensing calibrations are required to constrain the magnitude of the hydrostatic equilibrium bias on the total cluster mass.

The baryonic content of the universe, while energetically small, is what makes up all physical objects in the universe, what drives astrophysical phenomena such as radiation and planetary formation, and what eventually gave rise to life. Yet, until recently, baryons have been overshadowed by dark matter as tools for studying cosmology of the low-redshift universe and the growth of large-scale structure. Our results show that the baryon distribution is an excellent proxy for the dark matter distribution, and represents a new way of approaching the growth and evolution of halos and structure in the universe.

Bibliography

Afshordi, N., Lin, Y.-T., Nagai, D., & Sanderson, A. J. R. 2007, Monthly Notices of the Royal Astronomical Society, 378, 293

Anderson, M. E., Bregman, J. N., & Dai, X. 2013, The Astrophysical Journal, 762, 106

Andersson, K., et al. 2011, The Astrophysical Journal, 738, 48

Arnaud, M., Pointecouteau, E., & Pratt, G. W. 2007, Astronomy and Astrophysics, 474, L37

Arnaud, M., Pratt, G. W., Piffaretti, R., Böhringer, H., Croston, J. H., & Pointecouteau, E. 2010, Astronomy and Astrophysics, 517, A92

Bahcall, J. N., & Spitzer, L. J. 1969, The Astrophysical Journal, 156, L63

Bahcall, N. A., & Kulier, A. 2014, Monthly Notices of the Royal Astronomical Society, 439, 2505

Battaglia, N., Bond, J. R., Pfrommer, C., & Sievers, J. L. 2013, The Astrophysical Journal, 777, 123

Behroozi, P. S., Conroy, C., & Wechsler, R. H. 2010, The Astrophysical Journal, 717, 379

Bennett, C. L., et al. 2003, The Astrophysical Journal Supplement Series, 148, 1

Bergeron, J. 1985, Astronomy and Astrophysics, 155, L8-L11 (1986)

Bialek, J. J., Evrard, A. E., & Mohr, J. J. 2001, The Astrophysical Journal, 555, 597

BICEP2 Collaboration et al. 2014, e-print arXiv:1403.3985, 19

Bode, P., Ostriker, J. P., & Vikhlinin, A. 2009, The Astrophysical Journal, 700, 989

Bonamente, M., Lieu, R., Mittaz, J. P. D., Kaastra, J. S., & Nevalainen, J. 2005, The Astrophysical Journal, 629, 192

Booth, C. M., Schaye, J., Delgado, J. D., & Dalla Vecchia, C. 2012, Monthly Notices of the Royal Astronomical Society, 420, 1053

Burns, J. O., Skillman, S. W., & O'Shea, B. W. 2010, The Astrophysical Journal, 721, 1105

Cen, R., Miralda-Escude, J., Ostriker, J. P., & Rauch, M. 1994, The Astrophysical Journal, 437, L9

Cen, R., & Ostriker, J. P. 1999, The Astrophysical Journal, 514, 1

Chen, H.-W., Helsby, J. E., Gauthier, J.-R., Shectman, S. A., Thompson, I. B., & Tinker, J. L. 2010, The Astrophysical Journal, 714, 1521

Dai, X., Bregman, J. N., Kochanek, C. S., & Rasia, E. 2010, The Astrophysical Journal, 719, 119

Dave, R., Hernquist, L., Katz, N., & Weinberg, D. H. 1999, The Astrophysical Journal, 511, 521

Dodelson, S. 2003, Modern Cosmology (San Diego: Academic Press)

D'Odorico, S., & Savaglio, S. 1991, Quasar Absorption Lines, Proceedings of the ESO Mini-Workshop held 20-21 February, 1991. Organized by P.A. Shaver, E.J. Wampler and A.M. Wolfe., p.51

Dunkley, J., et al. 2009, The Astrophysical Journal Supplement Series, 180, 306

Durrer, R. 2008, The Cosmic Microwave Background (New York, NY: Cambridge University Press)

Eckert, D., Ettori, S., Molendi, S., Vazza, F., & Paltani, S. 2013a, Astronomy & Astrophysics, 551, A23

Eckert, D., Ettori, S., Molendi, S., Vazza, F., Roncarelli, M., Gastaldello, F., & Rossetti, M. 2013b, e-print arXiv:1310.8389

Eckert, D., Molendi, S., Vazza, F., Ettori, S., & Paltani, S. 2013c, Astronomy & Astrophysics, 551, A22

Eckert, D., et al. 2012, Astronomy & Astrophysics, 541, A57

Eke, V. R., Cole, S., & Frenk, C. S. 1996, M.N.R.A.S., 282, 263-280 (1996)

Ettori, S., & Balestra, I. 2009, Astronomy and Astrophysics, 496, 343

Ettori, S., Morandi, A., Tozzi, P., Balestra, I., Borgani, S., Rosati, P., Lovisari, L., & Terenziani, F. 2009, Astronomy and Astrophysics, 501, 61

Giodini, S., et al. 2009, The Astrophysical Journal, 703, 982

Grego, L., Carlstrom, J. E., Reese, E. D., Holder, G. P., Holzapfel, W. L., Joy, M. K., Mohr, J. J., & Patel, S. 2001, The Astrophysical Journal, 552, 2

Gruen, D., et al. 2013, eprint arXiv:1310.6744, 36

Guo, Q., White, S., Li, C., & Boylan-Kolchin, M. 2010, Monthly Notices of the Royal Astronomical Society, 11

Gupta, A., Mathur, S., Krongold, Y., Nicastro, F., & Galeazzi, M. 2012, The Astrophysical Journal, 756, L8

High, F. W., et al. 2012, The Astrophysical Journal, 758, 68

Hinshaw, G., et al. 2013, The Astrophysical Journal Supplement Series, 208, 19

Hopkins, A. M., & Beacom, J. F. 2006, The Astrophysical Journal, 651, 142

Ichikawa, K., et al. 2013, The Astrophysical Journal, 766, 90

Iocco, F., Mangano, G., Miele, G., Pisanti, O., & Serpico, P. D. 2009, Physics Reports, 472, 1

Israel, H., Reiprich, T. H., Erben, T., Massey, R. J., Sarazin, C. L., Schneider, P., & Vikhlinin, A. 2014, e-print arXiv:1402.3267, 2

Kirkman, D., Tytler, D., Suzuki, N., OMeara, J. M., & Lubin, D. 2003, The Astrophysical Journal Supplement Series, 149, 1

Komatsu, E., & Seljak, U. 2001, Monthly Notices of the Royal Astronomical Society, 327, 1353

Lanzetta, K. M., Bowen, D. B., Tytler, D., & Webb, J. K. 1995, The Astrophysical Journal, 442, 538

Lau, E. T., Kravtsov, A. V., & Nagai, D. 2009, The Astrophysical Journal, 705, 1129

Linsky, J. L., Diplas, A., Wood, B. E., Brown, A., Ayres, T. R., & Savage, B. D. 1995, The Astrophysical Journal, 451, 335

Linsky, J. L., et al. 1993, The Astrophysical Journal, 402, 694

Mandelbaum, R., Seljak, U., & Hirata, C. M. 2008, Journal of Cosmology and Astroparticle Physics, 2008, 006

Martin, A. M., Papastergis, E., Giovanelli, R., Haynes, M. P., Springob, C. M., & Stierwalt, S. 2010, The Astrophysical Journal, 723, 1359

McCarthy, I. G., Bower, R. G., & Balogh, M. L. 2007, Monthly Notices of the Royal Astronomical Society, 377, 1457

McGaugh, S. S., Schombert, J. M., de Blok, W. J. G., & Zagursky, M. J. 2010, The Astrophysical Journal, 708, L14

Meléndez, J., & Ramírez, I. 2004, The Astrophysical Journal, 615, L33

Meneghetti, M., Rasia, E., Merten, J., Bellagamba, F., Ettori, S., Mazzotta, P., Dolag, K., & Marri, S. 2010, Astronomy and Astrophysics, 514, A93

Metzler, C. A., & Evrard, A. E. 1994, The Astrophysical Journal, 437, 564

Moster, B. P., Somerville, R. S., Maulbetsch, C., van den Bosch, F. C., Macciò, A. V., Naab, T., & Oser, L. 2010, The Astrophysical Journal, 710, 903

Mukhanov, V. 2005, Physical Foundations of Cosmology (New York, NY: Cambridge University Press)

Nagai, D., & Lau, E. T. 2011, The Astrophysical Journal, 731, L10

Nagai, D., Vikhlinin, A., & Kravtsov, A. V. 2007, The Astrophysical Journal, 655, 98

Navarro, J. F., Frenk, C. S., & White, S. D. M. 1996, The Astrophysical Journal, 462, 563

Nelson, K., Rudd, D. H., Shaw, L., & Nagai, D. 2012, The Astrophysical Journal, 751, 121

Niemann, H. B., et al. 1996, Science, 272, 846

Oppenheimer, B. D., Davé, R., Katz, N., Kollmeier, J. A., & Weinberg, D. H. 2012, Monthly Notices of the Royal Astronomical Society, 420, 829

Oppenheimer, B. D., Davé, R., Kereš, D., Fardal, M., Katz, N., Kollmeier, J. A., & Weinberg, D. H. 2010, Monthly Notices of the Royal Astronomical Society, 406, 2325

Ostriker, J. P., Peebles, P. J. E., & Yahil, A. 1974, The Astrophysical Journal, 193, L1

Peeples, M. S., Werk, J. K., Tumlinson, J., Oppenheimer, B. D., Prochaska, J. X., Katz, N., & Weinberg, D. H. 2014, The Astrophysical Journal, 786, 54

Planck Collaboration. 2011, Astronomy & Astrophysics, 536, A11

—. 2013a, e-print arXiv:1303.5062

—. 2013b, eprint arXiv:1303.5076

—. 2013c, Astronomy & Astrophysics, 558, C2

—. 2013d, Astronomy & Astrophysics, 550, A131

Prochaska, J. X., Weiner, B., Chen, H.-W., Mulchaey, J., & Cooksey, K. 2011, The Astrophysical Journal, 740, 91

Rasheed, B., Bahcall, N., & Bode, P. 2011, Proceedings of the National Academy of Sciences of the United States of America, 108, 3487

Ryden, B. 2003, Introduction to Cosmology (San Francisco: Addison Wesley)

Sargent, W. L. W., Young, P. J., Boksenberg, A., & Tytler, D. 1980, The Astrophysical Journal Supplement Series, 42, 41

Sheldon, E. S., et al. 2009a, The Astrophysical Journal, 703, 2217

—. 2009b, The Astrophysical Journal, 703, 2232

Somerville, R. S., & Primack, J. R. 1999, Monthly Notices of the Royal Astronomical Society, 310, 1087

Spergel, D., Flauger, R., & Hlozek, R. 2013, eprint arXiv:1312.3313

Steidel, C. C., Erb, D. K., Shapley, A. E., Pettini, M., Reddy, N., Bogosavljević, M., Rudie, G. C., & Rakic, O. 2010, The Astrophysical Journal, 717, 289

Steigman, G. 2006, International Journal of Modern Physics E, 15, 1

Sun, M., Voit, G. M., Donahue, M., Jones, C., Forman, W., & Vikhlinin, A. 2009, The Astrophysical Journal, 693, 1142

Sunyaev, R. A., & Zeldovich, Y. B. 1972, Comments on Astrophysics and Space Physics, Vol. 4, p.173

Suzuki, T. K., Yoshii, Y., & Beers, T. C. 2000, The Astrophysical Journal, 540, 99

Takizawa, M., & Mineshige, S. 1998, The Astrophysical Journal, 499, 82

Thom, C., et al. 2012, The Astrophysical Journal, 758, L41

Tumlinson, J., et al. 2011, Science (New York, N.Y.), 334, 948

Tytler, D., Fan, X. M., & Burles, S. 1996, Nature, 381, 207

Umetsu, K., et al. 2009, The Astrophysical Journal, 694, 1643

Vikhlinin, A., Kravtsov, A., Forman, W., Jones, C., Markevitch, M., Murray, S. S., & Van Speybroeck, L. 2006, The Astrophysical Journal, 640, 691

von der Linden, A., et al. 2014, ArXiv e-prints

Weinberg, S. 2008, Cosmology (New York, NY: Oxford University Press)

Werk, J. K., Prochaska, J. X., Thom, C., Tumlinson, J., Tripp, T. M., O'Meara, J. M., & Peeples, M. S. 2013, The Astrophysical Journal Supplement Series, 204, 17

Werk, J. K., et al. 2014, e-print arXiv:1403.0947, 19

Zhu, G., & Ménard, B. 2013, The Astrophysical Journal, 773, 16